

POLITECNICO DI TORINO

Collegio di Ingegneria Meccanica e Aerospaziale

**Corso di Laurea Magistrale
in Ingegneria dell'Autoveicolo**

Tesi di Laurea Magistrale

**FE Simulation of the Hole Expansion
Experimental Test of High Strength
Aluminum Alloys**



Relatore

Prof. Giovanni Belingardi

Co-Relatore

Prof. Michael J. Worswick

Candidato

Enrico Lai

A.A. 2019/2020

ABSTRACT

Edge failure is one of the major problems associated with forming operations of metal sheets. During recent years, some Aluminum Alloys, as AA7075, are gaining attention and interest in academia due to their increasing utilization in manufacturing processes, especially in the automotive. As a result, there is an interest in developing numerical techniques able to predict the edge failure in forming simulations and consequently optimize the forming operations in the automotive industry for vehicle light-weighting, in agreement with the most recent regulations.

The stretch-flangeability of AA7075-T6 were predicted with FE hole expansion simulations involving different boundary conditions, as temperature and punch shape variations.

The standard conical punch as well as a custom flat punch were used to investigate how punch shape affects the formability when the hole is expanded out-of-plane (conical punch) and in-plane (flat punch). The effect of temperature was investigated considering simulations at room and warm conditions (25 and 200 Celsius degrees respectively).

The primary objective of this thesis is then, basing on the available experimental data, to build a Finite Element Model (FEM) able to characterize the induced strain and stress within the metal blank during the various test condition and predict the failure of the blank. The FEM is also useful to assess if the material tensile properties affect the edge stretchability of the hole and in which way; in fact, the relationship between hole expansion simulations results and tensile-mechanical properties were developed for both conditions.

Comparing the predicted results of the simulations with other aluminum alloys analyzed in previous literature, it was found that the AA7075-T6 shows a relatively high edge sensitivity in the hole expansion simulations with the conical punch (HER = 28% at room temperature, HER = 35% at warm temperature), with a predicted fracture in pure uniaxial stress on the edge for both the room and the warm condition; on the contrary, the expansion with the flat punch shows the most critical point some millimeters away from the hole edge, in a zone that presents plane values (HER = 19% at room temperature, HER = 24% at warm temperature).

ACKNOWLEDGEMENTS

First, I would like to thank the FCA Group for offering me the possibility to attend a six-month internship in Canada with their economic support.

I would like to express my gratitude to the University of Waterloo for the hospitality, in particular to Prof. Michael Worswick for giving me the great opportunity to work on this research project and to be part of his workgroup during the writing of this work. His patience and continuous support during the last months have been essential to me, especially considering the circumstances related to the pandemic.

I also would like to express my profound acknowledgment to all the other members of the Prof. Worswick's research group: the technicians, the assistants, the researchers, the post-docs, the Ph.D. and the MSc students, for the daily help and for making me feel part of their group, it was a pleasure. In particular, I would like to thank Laurie Wilfong, Sante DiCecco, Jaqueline Noder, Tamjeed Rahmaan, and Advait Narayanan for the technical support in the writing of this work. I would like to dedicate special mention for the EC4 "coffee gang" and for the classmates of ME725.

I also would like to thank Prof. Belingardi, which in recent months has always provided technical and moral support from the Polytechnic of Turin, following the developments of this period abroad and supervising my activities with great care.

I would like to thank the many friends that I have come across during these university years that helped me in the most various ways and have been a source of continuous support and inspiration. I cannot mention individually all of you, the length of this work would not be enough!

Last but not least, a special thanks to my (large) family, for everything.

*A mia madre Laisa,
Ti voglio bene.*

Table of Contents

ABSTRACT	iii
ACKNOWLEDGEMENTS	iv
List of Figures.....	viii
List of Tables.....	xi
1 INTRODUCTION.....	1
1.1 Aluminum alloys.....	1
1.2 Warm forming and aluminum.....	3
1.3 Aluminum Alloys in Automotive Industry.....	6
2 LITERATURE REVIEW	10
2.1 Shearing process and characteristics of the sheared edge	10
2.2 Sheared Edge Stretching-limit.....	12
2.3 Anisotropy	14
2.4 Strain hardening model.....	15
2.5 Temperature and strain rate effect	16
2.5.1 Temperature and strain rate effect on AA7075 – T6.....	17
2.6 Plastic instability and necking	18
2.7 Yield criteria	19
2.8 Ductile material damage model.....	22
2.9 Heat treatment.....	24
2.9.1 Heat treatment AA6xxx.....	26
2.9.2 Heat treatment AA7xxx.....	26
2.10 Lubricants	27
3 OBJECTIVES OF THE WORK	29
4 FINITE ELEMENT SIMULATION	30
4.1 Description of the actual forming process being modelled	30
4.2 Purpose of the simulation	31

4.3 Model description	31
4.3.1 Modelling approach.....	31
4.3.2 Geometry and Element type selection and rationale	32
4.3.3 Material model adopted	33
4.3.4 Boundary conditions.....	38
5 RESULTS.....	41
5.1 Room temperature hole expansion results.....	45
5.1.1 In-plane strains	45
5.1.2 Thickness strain distribution.....	47
5.1.3 Triaxiality distribution and MCC	48
5.2 Warm Temperature Hole Expansion results.....	51
5.3 Punch force vs displacement	56
5.4 Correlation of Hole Expansion with Tensile Properties	57
6 CONCLUSIONS & FUTURE WORK.....	60
6.1 Conclusions	60
6.2 Future work	62
Bibliography	65

List of Figures

Figure 1 - Price graph of aluminum (US\$/ton) at the London Metal Exchange, cash buyer contract type (lme.com, 2020).....	4
Figure 2 – Temperature-dependent forming limit curves for aluminum AA7075-T6 alloy, 2 mm thickness. Adapted from Sotirov et al. (2012).	5
Figure 3 - Trend of Net Aluminum Content in North American light vehicle record and forecast (Ducker, 2017).....	7
Figure 4 – Detail of the materials used for BIW and closures and their contribution to overall car weight (EuroCarBody, 2016).....	8
Figure 5 – Exploded view of the Ford F–150 (2015) body components	9
Figure 6 - A schematic representation of the shear edge in ductile materials (Seo, 2005)	10
Figure 7 a) - Schematic representation of the characteristic sheared edge of AA6xxx series for small cutting angles and/or clearances in which is present a secondary burnish area. b) – Detail of the sheared edge of an AA6xxx with 5% clearance, 0° cutting angle, 25.4µm blade edge radius (Li, 2000)	11
Figure 8 – Schematic representation of hole expansion test in the initial (a) and deformed (b) states (Pathak et al., 2016).	12
Figure 9 – Schematic representation of stress state in an element along the hole edge (Liu et al., 2018).12	
Figure 10 - True stress-true strain curves of 7075-T6 aluminum alloy deformed at (a) various temperatures with a constant strain rate of 0.058 s ⁻¹ and (b) different strain rates with a constant temperature of 220°C (Wang et al., 2012).....	17
Figure 11 - Normalized yield criteria comparison (M. Worswick, ME725 course slides 2020)	21
Figure 12 - Ductile material failure mechanism	22
Figure 13 - Heat treatment of a 2xxx aluminum alloys in which are present the three main phases of the process: 1) solution treatment, 2) quench, 3) aging (Source: NDT Resource Center).	24
Figure 14 – Quarter model used for the simulation.....	31
Figure 15 - Detail of the punch geometries used in the simulation	32
Figure 16- Detail of the workpiece mesh with a highlight on the three zones	33
Figure 17 - Predicted Barlat YLD2000 yield surface for AA7075 – T6 sheet at plastic logarithmic strains of 0.08 in tensile test in the rolling direction (Rahmaan et al., 2016).....	35
Figure 18 - Flow stress of AA7075-T6 along rolling direction at 25°C used in the simulation. Experimental data from Rahmaan et al. (2016).....	36
Figure 19 - Set of stress-strain relations used in the thermal-mechanical FE model based on Wang et al. (2012) data reported in Figure 10.	37
Figure 20 - Detail of symmetry boundary conditions applied on the workpiece	38
Figure 21- Punch displacement vs time	39
Figure 22 - Binder displacement vs time.....	40

Figure 23 – Conical Hole Expansion simulation, effective stress (von-Mises) contour at the failure time according to FLSD.....	42
Figure 24 - Flat Hole Expansion simulation, effective stress contour at the failure time according to FLSD	43
Figure 25 - Selected elements for the strain analysis along workpiece rolling direction. a) Point A and B location on the conical expansion blank. b) Point A to point G location on the flat expansion blank.	43
Figure 26 - Forming Limit Stress Curve AA7075-T6 at 25°C. In the conical expansion, the element on the edge is the first to reach the stress limit; in the flat expansion, the point B is the first. The element labels refer to Figure 25a and Figure 25b for the conical and flat case, respectively.	44
Figure 27 - Forming Limit Stress Curve AA7075-T6 at 200°C. The element labels refer to Figure 25a and 25b for the conical and flat case, respectively.....	45
Figure 28 - Strain path of Conical Expansion, 25°C, at the hole edge (point A) and punch shoulder (point F). The element labels refer to Figure 25a (FLD source: Sotirov et al. (2012)).	46
Figure 29 - Strain path of Flat Expansion, 25°C, from the hole edge (point A) to the punch shoulder (point G); (FLD source: Sotirov et al. (2012)).	47
Figure 30 - Thickness reduction along the rolling direction from the hole edge up to 8mm, for both the conical and flat expansion workpieces.	48
Figure 31-Contourn of stress triaxiality within the workpiece on the conical expansion, 25°C.	49
Figure 32 - Contour of stress triaxiality within the workpiece on the flat expansion, 25°C.....	49
Figure 33 - MCC AA7075-T6 (Source: Rahmaan, 2020).....	50
Figure 34 - MCC AA7075-T6 (Source: Rahmaan, 2020).....	51
Figure 35 – Temperature evolution of elements A, B, C of the blank up to 180 seconds since the clamping. Element labels refer to Figure 36.....	52
Figure 36 – Temperature gradient within the blank after 180 seconds since the clamping.....	52
Figure 37- Thermal stress induced in the blank due to warming.....	53
Figure 38 - Strain path of Conical Expansion, 200°C, from the hole edge (point A) to the punch shoulder (point F). The element labels refer to Figure 25a (FLD source: Sotirov et al. (2012)).	53
Figure 39 - Contour of stress triaxiality within the workpiece on the conical expansion, 200°C.	54
Figure 40 - Strain path of Conical Expansion, 200°C, from the hole edge (point A) to the punch shoulder (point F). The element labels refer to Figure 25b (FLD source: Sotirov et al. (2012)).	55
Figure 41- Contour of stress triaxiality within the workpiece on the flat expansion, 200°C.	56
Figure 42- Force exchanged between the punch and the workpiece vs the punch displacement considering different punches and temperatures.....	57
Figure 43- Effect of transverse total elongation on percent hole expansion. AA7075-T6 data based on the Rahmaan et al. (2016) characterization effort. (Picture source: Adamczyk & Michal, 1986).	58
Figure 44 - Effect of r_m and transverse total elongation on percent hole expansion from linear regression analysis. AA7075-T6 data based on the Rahmaan et al. (2016) characterization effort. (Picture source: Adamczyk & Michal, 1986).	58

Figure 45- Relation between tensile strength and HER of AA7075-T6 with various steel tested by Manikandan et al. (2012). AA7075-T6 data based on the Rahmaan et al. (2016) characterization effort.59

Figure 46 - Correlation between HER (%) and tensile properties of AA7075-T6 and a variety of other materials: a) yield stress, MPa. b) ultimate tensile stress, MPa. AA7075-T6 data based on the Rahmaan et al. (2016) characterization effort. (Picture source: Paul, 2014b).59

List of Tables

<i>Table 1- Overview of different aluminum series and their characteristics (Kaufman, 2000)</i>	2
<i>Table 2 - Temper for heat treatment of wrought aluminum alloys (Kaufman, 2000)</i>	3
<i>Table 3 - Material properties of steels assigned to the tools</i>	33
<i>Table 4 - AA7075-T6 Mechanical properties used in the simulation at 25°C (Rahmaan, 2016)</i>	34
<i>Table 5 - Yld2000-2d parameters (Equation 2.20) for AA7075-T6 sheets proposed by Rahmaan et al. (2016)</i>	34
<i>Table 6 - Thermal material properties assigned to the tooling and the blank in the FE model (Source: Thermtest.com)</i>	36
<i>Table 7 - Predicted Hole Expansion Ratio for conical and flat expansion at 25°C and 200°C</i>	45

1 INTRODUCTION

The use of aluminum alloys in the automotive industry has increased significantly during the last decade due to their high strength-to-weight ratio and other properties that allow reduction of the vehicle mass and consequently the fuel consumption and the noxious gas emissions. On the other hand, the introduction of these alloys has introduced several technical issues in the manufacturing processes that need to be overcome in order to exploit the full potential of the material.

One of the issues that require special attention, and on which this work focuses, is that of the edge cracking, a difficult phenomenon to predict in advance. In fact, shearing of aluminum metal sheets is a very common manufacturing operation in the automotive and aircraft industries, this process alters the properties of the material on the sheet edges due to the non-uniform deformation. It results that a non-negligible portion of the sheet formability is lost at the edge and this may lead to premature failure during subsequent forming operations. Producing a machined edge would increase the workpiece formability but at the expense of production cost and time.

A useful measure of a material susceptibility to the edge cracking is the Hole Expansion Ratio (HER). Currently, HER is evaluated according to the standard test ISO16630:2017 (ISO/TS, 2017) in which a hole is introduced via punching on the sheet, and then expanded till the failure with a conical punch.

In this work, several Aluminium alloys, both 6xxx and 7xxx series, have been subjected to the Hole Expansion Test (HET) in different test conditions, including variations in cutting clearance, punch geometry, thermal conditions, in order to determine the Hole Expansion Ratio (HER) parameter and characterize the shear edge sensitivity of the material alloys.

1.1 Aluminum alloys

The employed alloy designation system is based on the *Aluminum Association Inc.* four-digit method for wrought aluminum. The first number identifies the major alloying element and defines the aluminum series, whereas the second one gives information on the modification number. The third and fourth digit are arbitrary numbers for identification of the specific alloy in the series (Kaufman, 2000). An overview of these

different series, their principal alloying elements, and their major characteristics are given in Table 1.

Table 1- Overview of different aluminum series and their characteristics (Kaufman, 2000)

SERIES	MAJOR ALLOYING ELEMENT(S)	MAJOR CHARACTERISTICS
1XXX	Pure aluminum (min 99%)	Strain hardenable, corrosion-resistant, high formability, and electrical conductivity. UTS: 70 ÷ 185 MPa
2XXX	Copper	Heat treatable (precipitation hardening), fatigue resistant. UTS: 190 ÷ 430 MPa
3XXX	Manganese	High formability, corrosion-resistant, strain hardenable. UTS: 110 ÷ 285 MPa
4XXX	Silicon	Heat treatable, good flow characteristics. UTS: 175 ÷ 380 MPa
5XXX	Magnesium	Strain hardenable, good corrosion-resistant, toughness, and weldability. UTS: 125 ÷ 350 MPa
6XXX	Magnesium – Silicon	Heat treatable, high corrosion resistance, good machinability. UTS: 125 ÷ 400 MPa
7XXX	Zinc	Heat treatable, excellent strength. UTS: 220 ÷ 610 MPa
8XXX	Lithium and other elements (mixed alloys)	Heat treatable, high strength, low density. UTS: 120 ÷ 240 MPa
9XXX	Experimental	No general properties.

The addition of alloying elements affects the aluminum alloys properties in terms of strength, corrosion resistance, and conductivity. The aluminum alloy series can be further distinguished in terms of the ability to undergo heat treatment that includes

2xxx, 6xxx, and 7xxx series, with 4xxx depending on the specific alloy. In Table 2 an overview of the heat treatment designation of wrought aluminum alloys is reported.

Table 2 - Temper for heat treatment of wrought aluminum alloys (Kaufman, 2000)

TEMPER	DEFINITION
T1	Cooled from an elevated temperature shaping process and naturally aged
T2	Cooled from an elevated temperature-shaping process, cold worked, and naturally aged
T3	Solution heat treated, cold worked, and naturally aged
T4	Solution heat treated and naturally aged
T5	Cooled from an elevated temperature-shaping process and artificially aged
T6	Solution heat treated and artificially aged
T7	Solution heat treated and artificially over-aged
T8	Solution heat treated, cold worked, and artificially aged
T9	Solution heat treated, artificially aged, and cold worked
T10	Cooled from an elevated temperature shaping process, cold worked, and artificially aged

1.2 Warm forming and aluminum

For a long time, the use of medium-strength aluminum alloys (5xxx and 6xxx series) for structural components of cars such the B-pillar, has been not competitive compared to the usage of hot-stamped ultra-high strength (UHSS) steels (Hui *et al.*, 2012). Moreover, the heat treatable aluminum alloys series 6xxx and 7xxx, reach their maximum strength when they are subjected to a precipitation process, with the possible drawback to being exposed to further precipitation coarsening phenomena (over-aging) if exposed to high temperature, corresponding to a decrease in strength.

7xxx series aluminum alloys do offer higher strength levels (and a strength-to-weight ratio comparable to UHSS), however, these alloys have low formability and multi-step forming processes with intermediate heat treatments are required to overcome forming issues such as thermal distortion, excessive spring back, or changes in the microstructure. These additional operations, along with the high cost of these alloys, until some years ago, contributed to consider the use of this material as a costly solution. In recent years, the cost of aluminum has steadily decreased (Figure 1) as a consequence of the increased

adoption of this material in automotive fabrication (high demand) and the consequent increase in production volume.

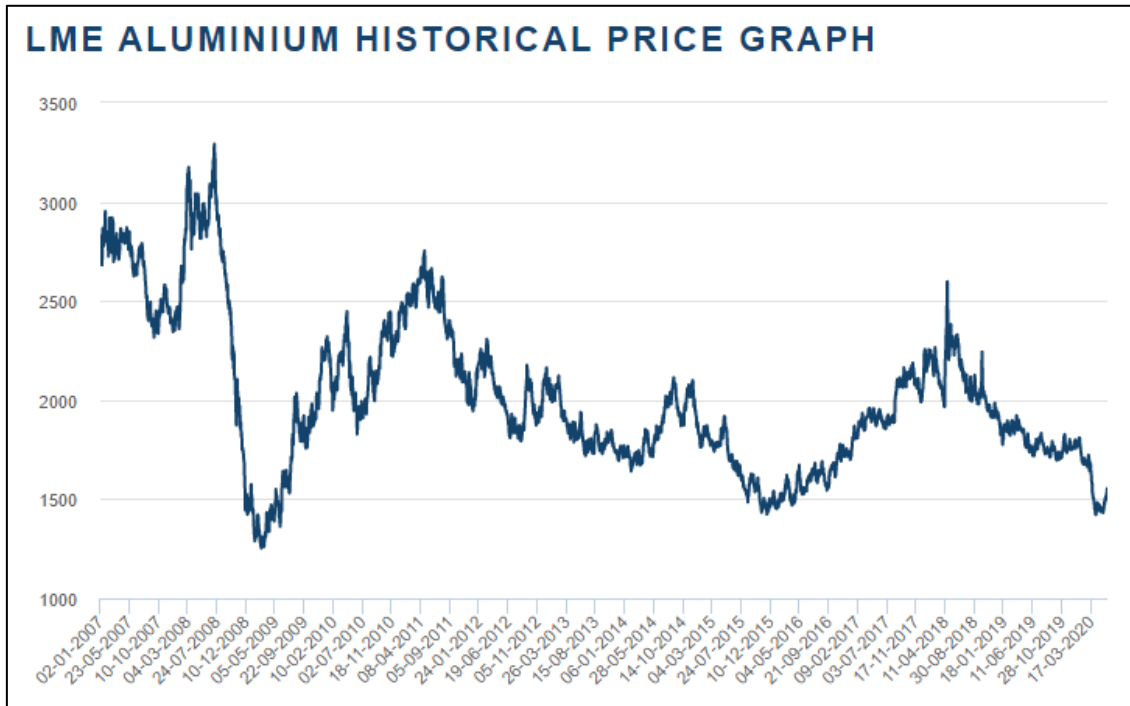


Figure 1 - Price graph of aluminum (US\$/ton) at the London Metal Exchange, cash buyer contract type (lme.com, 2020)

An option to overcome the limited formability of high strength aluminum alloys is warm forming, however, heat exposure must be limited to prevent changes to the microstructure that would result in a drop of the final part strength and would also affect the corrosion performance. Forming limit curves represent the critical major strain, as a function of minor strain, at which necking/cracking is observed under different loading conditions and serves to compare the formability of materials. A material that can sustain higher major strains before necking exhibits better formability. Aluminum alloys are generally characterized by limited formability at room temperature that can be improved at elevated temperatures as demonstrated by Sotirov *et al.* (2012) and DiCecco (2020) for AA7075-T6, as shown in Figure 2.

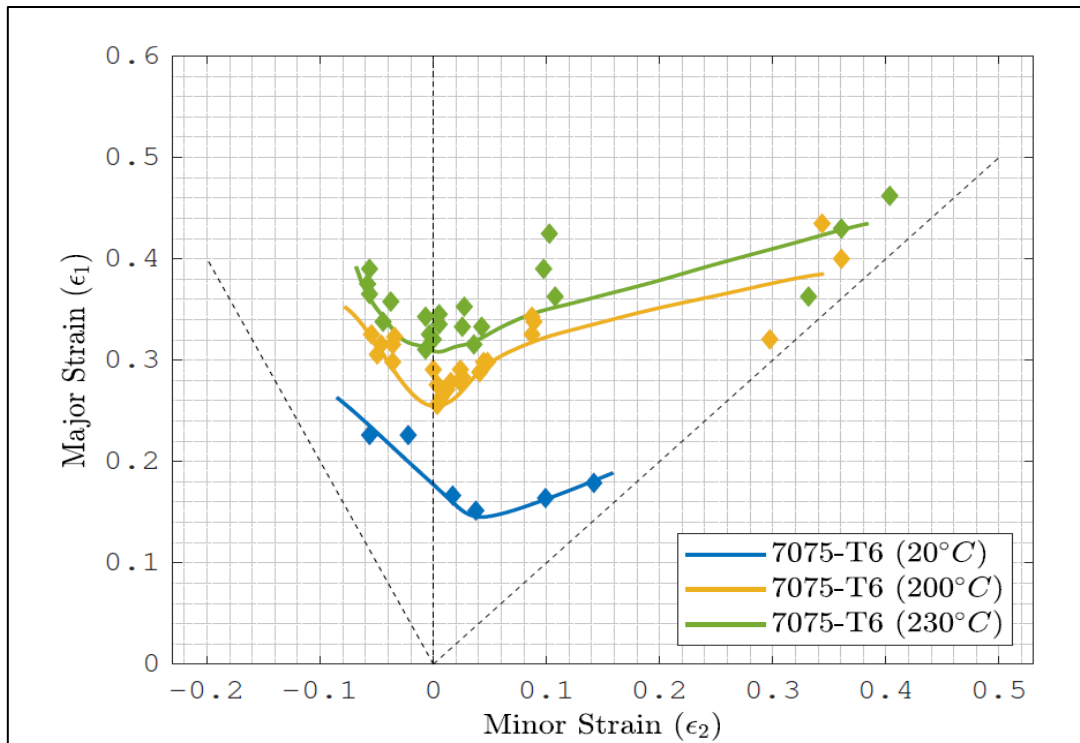


Figure 2 – Temperature-dependent forming limit curves for aluminum AA7075-T6 alloy, 2 mm thickness. Adapted from Sotirov *et al.* (2012).

To compensate for the inferior formability of aluminum, compared to mild steel, researchers as Garret *et al.* (2017) have been looking into alternative forming processes such as die quenching, in which the material is at first heated to elevated temperature (range of 470-560°C) to form a homogeneous solid solution, and then rapidly formed in a cooled die. After die quenching the material is in a so-called W-temper (fully solutionized) and natural or artificial aging treatments are required to reach full-strength that can be costly and lengthy.

As an alternative to die quenching, warm forming at temperatures below the material recrystallization temperature (typically less than 300°C) represents an attractive alternative.

Compared to conventional cold forming, elevated temperature warm forming incurs higher costs due to a more complex die design to incorporate electrical heaters, higher energy consumption, increased tool wear, and changing process parameters such as the use of high-temperature lubricants. Heating the blank and keeping the tooling at room temperature yields cost-savings and could extend the process window, as pointed out by Toros *et al.* (2012).

Morris and George (1977) pioneered application of warm forming to full-scale structural parts produced at Chrysler Corporation (now Fiat Chrysler Automobiles N.V.) for selected 5xxx series work-hardened alloys and peak-aged 6xxx and 7xxx series age-hardened alloys. They highlighted the importance of short heating cycles (on the order of one to two minutes by means of an infrared heater) in combination with a lubricant to prevent rapid cooling and found the black color of a resin bonded graphite lubricant beneficial in minimizing heat reflection. To prevent formability problems, the blank has to be formed fast enough before the temperature drops below a critical value. From tensile baseline studies, they found 200°C as an optimal forming temperature for age-hardened aluminum alloys in view of bending and drawing operations. They reported that the benefits were reduced in stretching operations of age-hardened alloys due to a reduced strain-rate hardening at elevated temperature that controls diffuse necking.

1.3 Aluminum Alloys in Automotive Industry

In working to meet governmental legislative requirements for automotive vehicle emissions and fuel economy standards, the automobile industry is challenged to minimize fuel consumption while maintaining comfort and driving performance.

The automotive industry identified the use of light materials as good compromise between the above-mentioned various requirements. In the last years, aluminum alloys have gained particular interest as vehicle structural materials to reduce weight, due to their mechanical properties. The most attractive properties are the high strength-to-weight ratio, good corrosion resistance, and excellent thermal and electrical conductivity. The large interest by the automotive industry for this material is projected in the steady increase in the fraction of aluminum alloys making up the vehicle body, as shown in Figure 3 (Ducker, 2017).

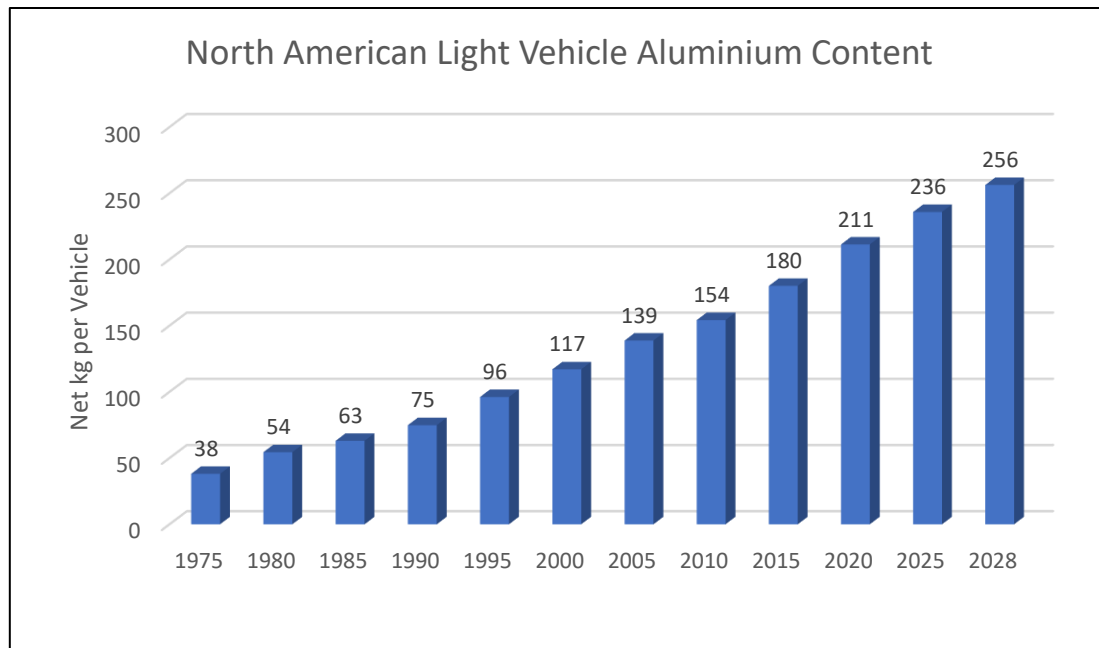


Figure 3 - Trend of Net Aluminum Content in North American light vehicle record and forecast (Ducker, 2017)

Large content increases for closures, body-in-white parts, and crash management parts are driving nearly 30 kg of net aluminum content growth from 2015 to 2020 (Ducker, 2017).

An example of how carmakers are investing in aluminum alloys in order to accomplish weight reduction is the Giulia, presented in 2016 by Alfa Romeo, in which AA5xxx and AA6xxx series sheets were chosen for the closures and other components in the car body (Figure 4). Considering only the body in white and the closures, the various aluminum components account for the 16% of the total weight, generating a weight reduction of 13% relative to an equivalent body made using steel (ilprogettistaindustriale.it, 2017). Taking in consideration the only closures, made by AA6xxx series sheets, accounts for 25 kg mass reduction on the overall.

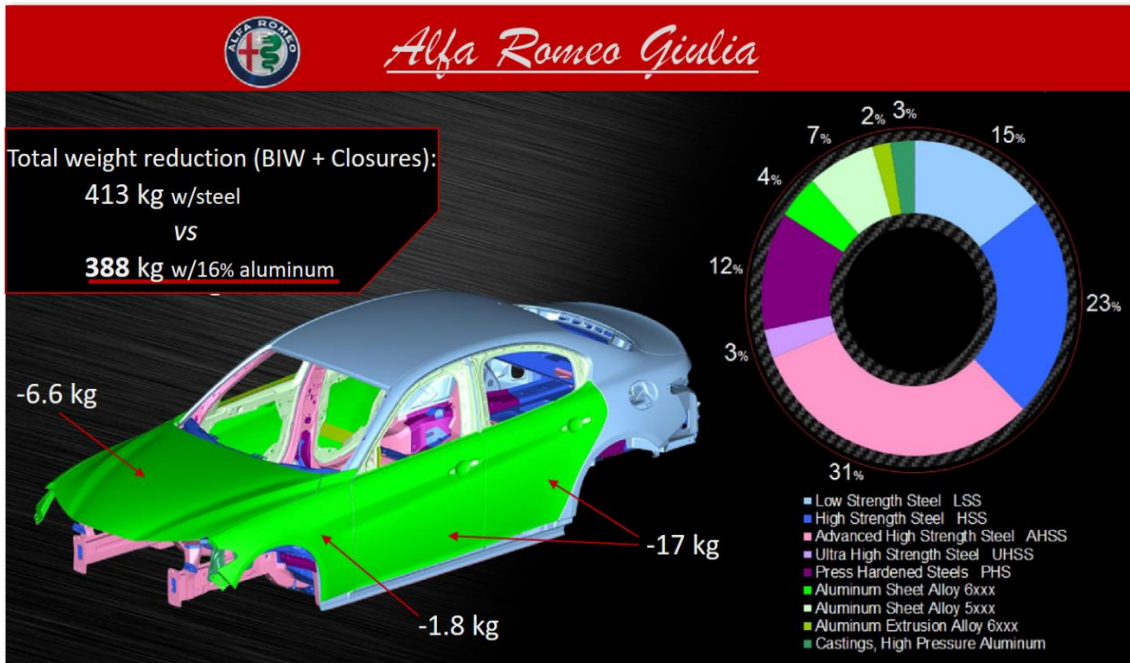


Figure 4 – Detail of the materials used for BIW and closures and their contribution to overall car weight (EuroCarBody, 2016)

Considering the North American automotive market, along with new fuel economy regulations that will require the U.S. vehicle fleet to average 54.5 miles per gallon (4.3l per 100km) by 2025, the auto industry is responding. An iconic example is the Ford’s all-aluminum-body F-150 pickup truck (Figure 5). This move toward aluminum has profound implications since the Ford F-150 is the most popular vehicle of any kind in the United States and one of the most profitable motor vehicle lines in the world. The 2015 F-150 truck shed 300 kg (approximately 15% in vehicle body-weight) with a high-strength all-aluminum body (series 6xxx). The widespread research and development in car weight reduction enables carmakers to make other design changes, like smaller engines, that can further boost fuel economy (aluminum.org, 2020).

2 LITERATURE REVIEW

In this chapter the previous research results, that are inherent to the main topic of this work, are reported.

2.1 Shearing process and characteristics of the sheared edge

In a shearing process, a punch is used to push a blank against a die, which is fixed, and separates the sheet metal in two pieces at the edge of the shearing punch and die. The clearance, defined as the gap between the die and the punch, is an important variable that must be taken into account in the process and it is generally expressed as a percentage of the sheet thickness (Pathak, 2017).

The shearing processes of a metal sheet introduces two zones: a shear face (sheared edge) and a zone of deformation behind the shear face known as the shear-affected zone (SAZ).

In Figure 6 is shown a typical sheared edge composed of four zones: rollover zone, burnish zone, fracture zone, shear burr (Seo, 2005).

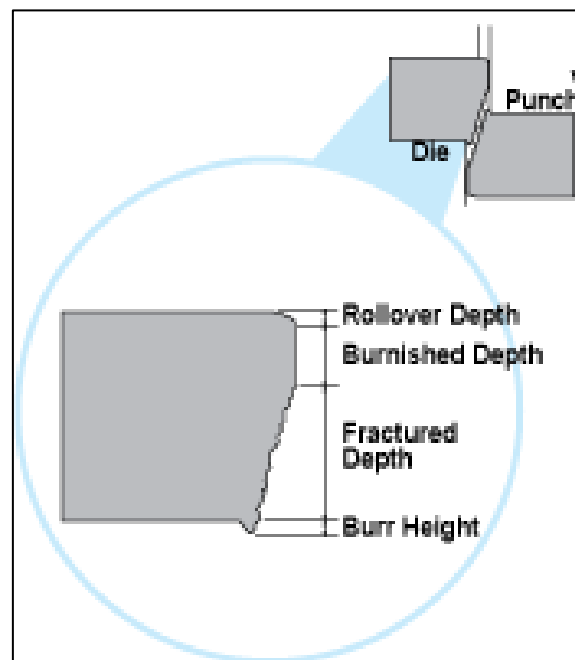


Figure 6 - A schematic representation of the shear edge in ductile materials (Seo, 2005)

Typically, during the shearing process, as the punch initially engages the metal sheet, it pulls the workpiece downward, slightly drawing the material into the clearance, which creates a rollover zone.

As the punch continues to penetrate and shear the upper portion of the material, the material becomes locked between the punch and the die, which creates a burnished area before the remaining material is fractured or separated.

The shear burr is formed at the intersection of the fracture area and the surface of the sheet in contact with the punch. In contrast with the other shear zones, the orientation of the shear burr with respect to the punch during Hole Expansion Test (HET) influences the edge stretchability and gives rise to what is referred to as either blur-up or burr-down configurations of the test (Pathak, 2018).

For small cutting angle and/or clearance configurations, Li (2000) reported that AA6xxx series may exhibit a second burnish surface, as reported in Figure 7.

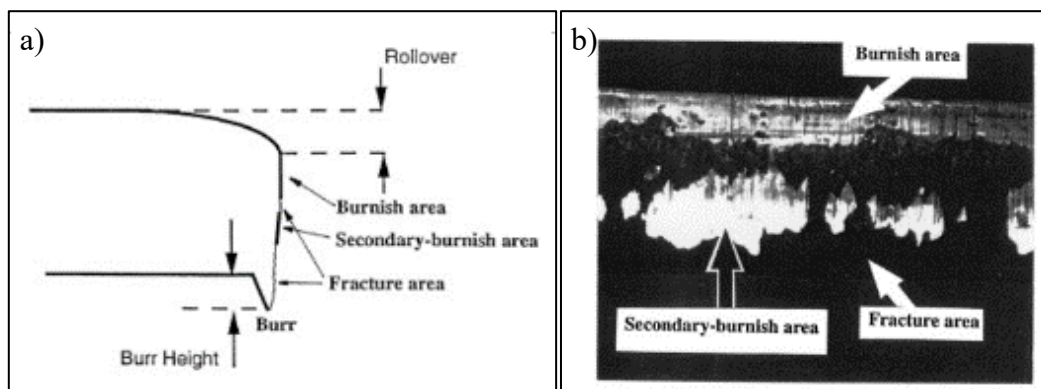


Figure 7 a) - Schematic representation of the characteristic sheared edge of AA6xxx series for small cutting angles and/or clearances in which is present a secondary burnish area. b) - Detail of the sheared edge of an AA6xxx with 5% clearance, 0° cutting angle, 25.4µm blade edge radius (Li, 2000)

While it is easy to notice the sheared edge defects just mentioned above, the SAZ is not visible just by looking at the sheared edge. This zone presents a severely work-hardened state that affects the formability of the sheared edge of the sheet in subsequent forming processes; this is the reason why is important to consider the effect of this zone in subsequent formability assessments. It is possible to determine the SAZ dimension with micro-hardness tests since the material hardness is an indicator of the strain-hardening; when the hardness measured from the edge saturates to a baseline value the SAZ limit is detected (Pathak N. , 2018).

It has been demonstrated that the shearing process also introduces micro-cracks on the blank edge that further reduce its formability since they could generate cracking (Seo, 2003).

2.2 Sheared Edge Stretching-limit

The Hole Expansion Test (HET) is commonly used to estimate the formability of material in stretch-flanging operations. The test, defined by the standard ISO 16630:2017 (ISO/TS, 2017), consists of the expansion with a punch of a 10mm hole pierced into a metal sheet (Figure 8). The test ends when a crack appears that has extended through the sample thickness. The Hole Expansion Ratio (HER) is the main result of the test expressed as the percentage ratio of the hole diameter variation to the original pierced diameter:

$$HER (\%) = 100 \left(\frac{d_f - d_0}{d_0} \right) \quad (2.1)$$

where d_0 is the initial hole diameter on the sample and d_f is the inside hole diameter at the fracture computed along 2 orthogonal directions. The ISO standard prescribes the use of a conical punch with a 60° included angle to expand the hole.

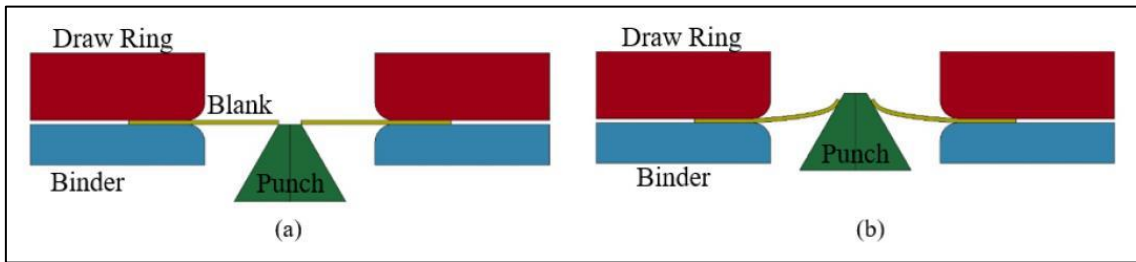


Figure 8 – Schematic representation of hole expansion test in the initial (a) and deformed (b) states (Pathak et al., 2016).

In the Hole Expansion Test, the hole is a free edge; in a simplified model, it is reasonable to assume that the deformation near the free edge follows a uniaxial stress path during the test since the main resultant stress is along the circumference as represented in Figure 9.

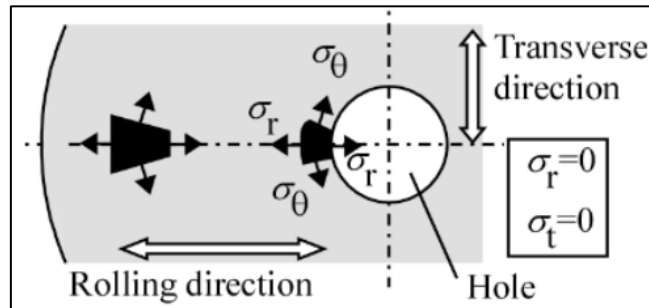


Figure 9 – Schematic representation of stress state in an element along the hole edge (Liu et al., 2018).

The correlation between the HER and several process parameters such as punch geometry, clearance of the shear dies and edge condition, have been well studied and

documented in the literature for steel sheet, while less literature is present for aluminum alloys. There are generic correlations between some parameters and the HER that are mostly either process-dependent or geometry-dependent and, not having at disposal specific results, they are often assumed as valid also for aluminum sheets.

Konieczny and Henderson (2007) considered several punch geometries for the HET on Advanced High Strength Steels (AHSS) and they obtained the highest expansion with the conical punch prescribed in the ISO-16630, while the lower HER was obtained with a flat punch. The same results were obtained by Pathak *et al.* (2016) and the difference in HER among the various punch geometries was explained by the different strain states developed during each test.

The edge conditions have been demonstrated to be one of the most important factors in the formability of a material. The formability of edges created using punching, milling and laser-cutting have been evaluated with the HET by Lee *et al.* (2007) and Konieczny and Henderson (2007) on AHSS. The best expansion ratio results were achieved with reamed holes.

During the years, the literature focused on the sheared edge and the SAZ features in order to assess the formability of metal sheets of different materials. Keeler (1971) and Smith (1990) showed an inverse relationship between HER and burr-height on AHSS. Levy and Van Tyne (2012) and Davies (1983) showed that by removing the SAZ (reaming process), the Hole Expansion Ratio increases. Bucher *et al.* (2014) using normalizing heat treatment in order to remove strain-hardening due to the cut operation, demonstrated that there are no significant differences between the normalized punched edge and a reamed one. Pathak *et al.* (2016) demonstrated with a comprehensive analysis of HET that work-hardening in the SAZ is the primary reason for reduced formability in the workpiece.

Stanton *et al.* (2011) tested 5xxx and 6xxx Aluminum alloys introducing the initial 10mm hole with several methods as punching, drilling and reaming, and CNC machining. They also combine the variety of samples with different punches typology during HET, obtaining an analytical expression that, according to some material parameters, allows to predict the HER for the considered materials with a margin of confidence within the typical experimental error. Stanton *et al.* (2011) also demonstrated the possibility to combine those alloys FLD with the results obtained from the HET.

The connection between the burr-height and the maximum elongation of the sheared edge has been investigated in the literature and the same inverse relationship found for AHSS were found also for 6xxx Aluminum alloys (Golovaschenko, 2008).

Bohdal et al. (2014) demonstrate the influence of clearance and trimming velocity on the sheared edge of AA6xxx series aluminum, describing how burr, fracture, burnish and rollover zones change as a function of these two variables.

2.3 Anisotropy

Sheet metals generally exhibit significant anisotropy in mechanical properties because of their crystallographic structure and the characteristics of (cold or warm) rolling process (Banabic, 2010). Most of these materials are orthotropic since the mechanical properties are symmetric with respect to three orthogonal axes. The parameters generally used to describe the anisotropy of a material are the Lankford parameter or anisotropy coefficient (Lankford et al., 1950), the coefficient of normal anisotropy (or normal anisotropy ratio), and the planar anisotropy coefficient.

The Lankford parameter, determined by uniaxial tensile test, links the different strain behaviors of the material along different directions:

$$R = \frac{\varepsilon_w}{\varepsilon_t} \quad (2.2)$$

Where ε_w and ε_t are the strain along the width and the thickness direction of the specimen, respectively. These values can be recorded along many directions of the sheet, generally 0° , 45° , and 90° assuming the rolling direction as the reference. By convention, these coefficients are usually determined at a particular level of elongation (*e.g.* 10-20%) in order to generalize the values among various materials (Banabic, 2010).

The coefficient of normal anisotropy (or normal anisotropy ratio), corresponding to an average value accounting for directional differences within the sheet plane, is defined as follow:

$$\bar{R} = \frac{R_0 + 2R_{45} + R_{90}}{4} \quad (2.3)$$

To describe the variation of the anisotropy coefficient within the sheet plane, the coefficient of planar anisotropy is commonly used:

$$\Delta R = \frac{R_0 + R_{90} - 2 R_{45}}{2} \quad (2.4)$$

If the Lankford parameter is greater than unity, it indicates that the width deformation is greater than the thickness deformation. This behavior generally means a higher resistance to the through-thickness strain and an improved sheet drawability. These parameters are usually helpful in predicting formability defects in the uniaxial strain field, such as wrinkling. However, they become meaningless in predicting limit strains under plane strain conditions, and fracture. For this purpose, the FLCs are required, or in the absence of data, the total elongation is more indicative than R-values.

As a general indication, BCC materials have a Lankford coefficient larger than unity (*e.g.* steels), while FCC materials tend to exhibit a value lower than the unit (*e.g.* aluminum alloys).

2.4 Strain hardening model

From a mechanical perspective, the micro-mechanisms of plastic deformation lead to increased resistance to further deformation. In sheet metal forming, it is essential to quantify the stress-strain relationship in the form of flow stress (σ_f) in order to capture the plastic behavior of the material and to simulate the forming process.

Many methods are capable to define a material flow curve, they can be classified into two main categories: phenomenological models and physically-based models. Phenomenological models fit the experimental results using non-physical parameters and their application is generally limited to the specific purpose of the application; on the other hand, physical based models are based on the micro-mechanics and physics of the material, and they provide a general description of the material in a wide range of application. For the purposes of this thesis, the phenomenological methods are sufficiently accurate to describe the strain-stress relation.

The model most widely used is known as power law:

$$\sigma_f = K \varepsilon^n \quad (2.5)$$

where σ_f is the flow stress, ε is the true strain, n is the strain hardening exponent, and K is a material coefficient.

This model, also known as Nadai model (Jones, 2009), is derived from the uniaxial tensile test and can be used expanded to the two-dimensional cases considering the equivalent strain (ε_{eq}).

This simple model can also be extended to take into consideration the effect of other variables as temperature and strain rate, which have a significant effect on the material flow stress. The more advanced Nadai model, known as the extended Nadai model (van den Boogaard *et al.*, 2001), is obtained by defining $n(T)$, $m(T)$, and $K(T)$ as a function of temperature:

$$\sigma_f = K(T)(\varepsilon + \varepsilon_0)^{n(T)} \left(\frac{Z(T)}{\dot{\varepsilon}_0} \right)^{m(T)} \quad (2.6)$$

where $Z(T)$ is the Zener-Hollomon parameter, $\dot{\varepsilon}_0$ is the reference strain rate, $m(T)$ is the strain rate sensitivity of the material, and the material coefficient $K(T)$ now evaluated as a function of temperature.

The Voce hardening function (Voce, 1955) is a three-parameter model commonly used to describe the flow stress of AA6xxx and AA7xxx series material:

$$\sigma_f = A - B * e^{-C\varepsilon_p} \quad (2.7)$$

Another function widely used to describe the hardening response of aluminum alloys is the Hockett-Sherby model, similar to the Voce model expressed in (2.7), in which the parameters n and D are included; the former is the exponent of the true plastic strain present in the second term of the equation, the latter multiply the square root of the true plastic strain in the third term:

$$\sigma_f = A - B * e^{-C\varepsilon_p^n} + D * \sqrt{\varepsilon_p} \quad (2.8)$$

Both the Voce and modified Hockett-Sherby models can be generalized in order to include the variation of the flow stress as function of the strain-rate and/or the temperature.

2.5 Temperature and strain rate effect

Temperature and strain rate have a significant effect on work hardening, and as a consequence, on formability. Temperature and strain rate generally have opposite effects on flow stress; as general trend, an increase in temperature corresponds to an increase in ductility and, with reference to equation 2.6, strain rate sensitivity parameter m , while both strength coefficient K and strain-hardening coefficient n decrease. On the other hand,

increasing the strain rate, the ductility decrease, and both strength coefficient K and strain hardening n increase.

2.5.1 Temperature and strain rate effect on AA7075 – T6

Recently, warm forming research has focused on high strength aluminum alloys, such as the AA7075-T6, in an effort to further reduce vehicle weight. Wang *et al.* (2012) investigated the forming response of AA7075-T6 basing his research on Nakazima dome-height measurements over a range of temperatures from 20°C to 260°C. AA7075-T6 has its highest UTS and the lowest total elongation at room temperature. Up to 100°C, only slight changes in mechanical properties are observed. In the range from 140°C to 220°C, UTS decreases, and maximum elongation increases. The sharp fall of mechanical properties noted at the highest temperature (260°C) was associated with over-aging. Figure 10a displays the stress-strain curves of AA7075-T6 at different temperature (range between 20°C and 260°C) and constant strain rate.

Wang *et al.* (2012) also investigated how strain rate affects the stress-strain relation of AA7075-T6, showing how decreasing the strain rate increases the ultimate elongation and reduces the UTS; they also noticed that the strain rate sensitivity parameter $m(T)$ increases up to 180°C and then slightly decreases. Figure 10b displays the stress-strain curves of AA7075-T6 under uniaxial deformation at various strain rates and constant temperature (220 °C).

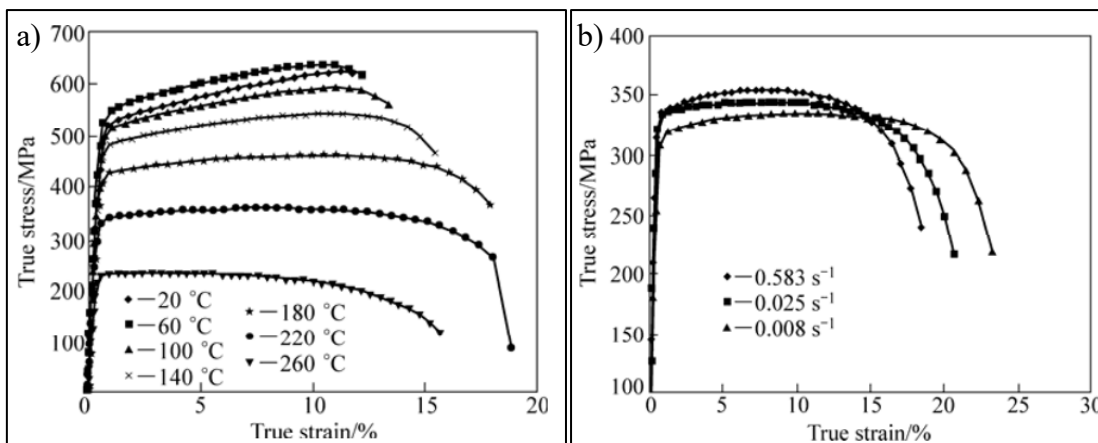


Figure 10 - True stress-true strain curves of 7075-T6 aluminum alloy deformed at (a) various temperatures with a constant strain rate of 0.058 s^{-1} and (b) different strain rates with a constant temperature of 220°C (Wang *et al.*, 2012).

2.6 Plastic instability and necking

In sheet metal forming processes, the onset of necking instead of fracture is usually regarded as the limit strain criterion since once localized necking occurs, the deformation process becomes unstable. Taking into consideration a uniaxial test at low strains, uniform deformation occurs along the full gage section.

Uniform extension is manifested during the tensile test assuming that the specimen section is the same along its length, physically and geometrically. If by chance, any region deformed more than the rest of the specimen, increased strength due to work hardening makes this anomalous deformation stop, until the rest of the specimen reaches an equivalent strain, at that point uniform deformation is re-established.

However, when the increase in stress due to the decrease in cross-sectional area becomes greater than the increase in load-carrying ability of the metal due to strain hardening, all deformation focuses within the necked section. In this condition, the deformation is unstable, and the localized strain rapidly evolves to fracture in the necked section (localization).

Numerous attempts to predict limit strains starting from physical and material considerations can be found in the literature. Some of these methods, properly calibrated, are currently used in FLD prediction in order to limit the amount of experimental work required to obtain FLCs.

Considère (1885) defined the criterion for the onset of localized necking in tensile tests based on strain hardening. In his analysis, the instability occurs at the peak load (engineering strain):

$$F = \sigma A \quad (2.9)$$

In the peak load condition, the derivative of the force is null ($dF = 0$):

$$dF = d\sigma A + \sigma dA = 0 \quad (2.10)$$

Arranging the equation and assuming volume constancy under plastic deformation:

$$\frac{d\sigma}{\sigma} = -\frac{dA}{A} = d\varepsilon \rightarrow \frac{d\sigma}{d\varepsilon} = \sigma \quad (2.11)$$

According to the Eq. 2.11, necking occurs when the derivative of the stress-strain curve is equal to the current stress value. Replacing the power-law (Eq. 2.5) in Eq. 2.9 results that diffuse necking happens when the strain reaches the value of the strain-hardening exponent n . However, these results are only valid in a uniaxial tension state; for this

reason, it has little applicability in the investigation of limit strains in sheet metal forming due to the wide range of strain paths encountered.

Swift (1952) provides a general criterion for localized necking in thin sheets under plane stress states. Hill showed that localized necking develops in the direction of zero-elongation. Thus, the strain component perpendicular to the necking direction is only due to sheet thinning. Hill's theory is in good accord with the experimental results in the drawing region of FLD (the left-hand side). Marciniak and Kuczynski (1967) developed a localized necking prediction theory known as the MK model. This model can predict the onset of localized necking in the biaxial stretching region of FLD (the right-hand side) based on the introduction of a pre-defined inhomogeneity in the metal sheet. In the MK model, usually, the defect is a small reduction in the initial thickness, but the model has been modified over the years to include other types of inhomogeneity in the material properties that might lead to necking.

2.7 Yield criteria

Yield criteria define the limit condition of the material elastic behavior, or in other words the onset of plastic deformation under multi-axial stress states. In multi-axial states of stress, the determination of plastic flow is not trivial and depends on all the values of stress tensor. This allows to define an implicit function, known as *yield function* (Banabic, 2010), that describes the stress states at which material deforms plastically:

$$F(\sigma_f, \sigma) = 0 \quad (2.12)$$

where all states that satisfy $F < 0$ correspond to elastic strain region and $F = 0$ corresponds to the material that undergoes plastic deformation. A state in which $F > 0$ has no physical meaning since the flow stress evolves with deformation.

Several theories are available in the literature for predicting the yield condition for both isotropic and anisotropic materials, all based on different hypotheses about the material behavior and resulting in yield functions of different shapes.

For isotropic material, the most common models are the *Tresca criterion* (Tresca, 1864) and the *Von Mises criterion* (Von Mises, 1913).

The Tresca criterion assumes that yield occurs when the maximum principal shear stress reaches a critical value, for the planar case it can be written as:

$$|\sigma_1 - \sigma_2| - \sigma_f = 0 \quad (2.13)$$

The equation 2.13 represents a polygon in the plane of principal stresses. The Von Mises criterion assumes that yield occurs when the elastic energy of distortion reaches a critical value, for plane stress it can be written in the form:

$$\sqrt{\sigma_1^2 + \sigma_2^2 - \sigma_1\sigma_2} - \sigma_f = 0 \quad (2.14)$$

the yield locus corresponds to an ellipse; due to the continuous shapes of the curve in principal stress planes, the Von Mises criterion is generally preferred for the numerical analysis.

On the other hand, to accurately describe anisotropic material behavior, anisotropic yield functions have been developed over the years. Hill (1948) proposed an anisotropic criterion as a generalization of the von Mises one assuming the yield function to be quadratic. Although the Hill criterion is simple, it does not work very well for aluminum alloys. Hill proposed then several non-quadratic functions able to extend the application of the criterion to more materials (Hill 1979, Hill 1987, Hill 1990, Hill 1990).

Another family of yield functions for anisotropic material is based on the work of Hershey (1954) and used for sheet materials. Examples of these models are a series of functions developed by Barlat and co-workers (Barlat and Lian 1989, Barlat et al. 1997a, 1997b, 2003, 2005). The criterion proposed by Barlat and Lian in 1989 provides a good prediction for aluminum alloys without high anisotropy. Rahmaan *et al.* (2016) show how the Barlat yield function YLD2000-2D (Barlat et al. 2003) provides a good description of the AA7075-T6 for sheet metal forming processes.

The yield function proposed by Barlat in 2000, called YLD2000-2d, utilizes two linear transformations of two isotropic yield functions that provide a higher number of anisotropy coefficients and allows more detailed description of the material behavior:

$$\Phi_{YLD2000-2d} = \Phi'(X') + \Phi''(X'') = 2\sigma_{eff}^a \quad (2.15)$$

where σ_{eff} is the effective material stress and the exponent a is chosen for the crystallographic structure of the material (normally 8 for face-centered (FCC) materials).

The anisotropic yield functions can be expressed as:

$$\Phi' = |X'_1 - X'_2|^a \quad (2.16)$$

$$\Phi'' = |2X''_2 - X''_1|^a + |2X''_1 - X''_2|^a \quad (2.17)$$

The linearly-transformed stress components in principal plane stress space can be obtained through Equation 2.18 where L' and L'' represent transformation tensors of the form recorded in Equation 2.191 and 2.20.

$$X' = L' : \sigma, X'' = L'' : \sigma \quad (2.18)$$

$$L' = \begin{bmatrix} L'_{11} & L'_{12} & 0 \\ L'_{21} & L'_{22} & 0 \\ 0 & 0 & L'_{66} \end{bmatrix}, \quad L'' = \begin{bmatrix} L''_{11} & L''_{12} & 0 \\ L''_{21} & L''_{22} & 0 \\ 0 & 0 & L''_{66} \end{bmatrix} \quad (2.19)$$

$$\begin{bmatrix} L'_{11} \\ L'_{12} \\ L'_{21} \\ L'_{22} \\ L'_{66} \end{bmatrix} = \begin{bmatrix} 2/3 & 0 & 0 \\ -1/3 & 0 & 0 \\ 0 & -1/3 & 0 \\ 0 & 2/3 & 0 \\ 0 & 0 & 1 \end{bmatrix} \begin{bmatrix} \alpha_1 \\ \alpha_2 \\ \alpha_3 \end{bmatrix}, \quad \begin{bmatrix} L'_{11} \\ L'_{12} \\ L'_{21} \\ L'_{22} \\ L'_{66} \end{bmatrix} = \frac{1}{9} \begin{bmatrix} -2 & 2 & 8 & -2 & 0 \\ 1 & -4 & -4 & 4 & 0 \\ 4 & -4 & -4 & 1 & 0 \\ -2 & 8 & 2 & -2 & 0 \\ 0 & 0 & 0 & 0 & 9 \end{bmatrix} \begin{bmatrix} \alpha_4 \\ \alpha_5 \\ \alpha_6 \\ \alpha_7 \\ \alpha_8 \end{bmatrix} \quad (2.20)$$

where α_i are anisotropic coefficients that are conventionally determined through uniaxial and equi-biaxial tension tests.

In Figure 11 a comparison of the most common yield criteria for the same material is reported.

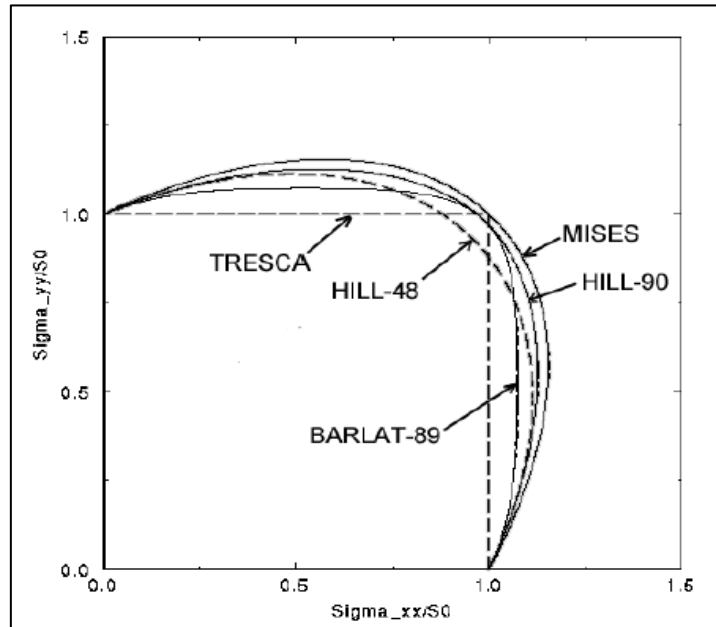


Figure 11 - Normalized yield criteria comparison (M. Worswick, ME725 course slides 2020)

2.8 Ductile material damage model

The fracture of ductile materials generally occurs through a process that involves nucleation, growth, and coalescence of microscopic voids, as illustrated in Figure 12.

Ductile materials, such as AA6xxx and AA7xxx series alloys, typically contain second phases and/or inclusions inside the matrix. When the material is subject to plastic deformation, due to the movement of the dislocations small cavities are generated in the material matrix (void nucleation). With the increase of the plastic deformation, the cavities grow until they coalesce each other and create micro-cracks. Micro-cracks grow and propagate, causing a softening in the material and localizing the stress, this phenomenon may lead to localizing neck and ultimately cause a failure. The damage in a material can be computed as the volume percentage of void in the aggregate material. It is important to understand the damage accumulation and fracture mechanism of a material in order to enhance their behavior during failure.

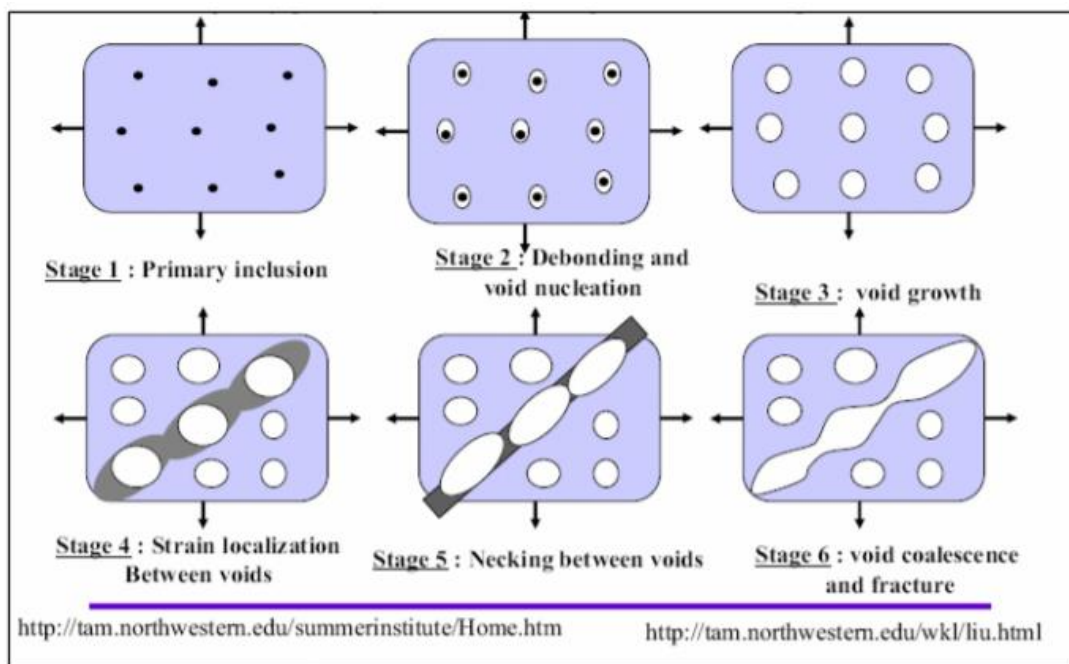


Figure 12 - Ductile material failure mechanism

As reported in the literature, the damage mechanism in 6xxx alloys typically stems from excessive plastic deformation (Lloyd, 1999) versus the gradual void nucleation and coalescence process in many other alloys. The uniform strain (the strain present before necking) is then mostly controlled by geometrical instability and it reflects the strain

dependence of the work hardening rate. This was studied experimentally for AA6111 - T4 by Hu *et al.* (2016) in which the samples from Hole Expansion Test shows very little physical damage (i.e. voids) near the fracture surfaces.

On the other hand, the 7xxx series generally shows a predominant ductile fracture mode under tensile deformation comprising microvoid nucleation, growth, and coalescence (Srivatsan *et al.*, 1997). Srivatsan *et al.* (1997) also studied the differences in microstructure and the tensile fracture mechanism at 27°C and 100°C.

The most accurate models that describe ductile material failure are micro-mechanics based; they are able to capture the material failure under non-proportional loading through prediction of void nucleation, growth and coalescence mechanism since failure is predicted as a consequence of microstructure (Pathak N. , 2018). The main drawback of the micro-mechanic approach is that it is very complex and requires a lot of studies to determine micro-mechanics characterization and modeling of the material.

In the literature, another method, based on the strain, has shown good results for the hole punching and expansion damage prediction. According to Hu *et al.* (2016), the material damage for AA6xxx in tension is assumed to follow a strain-based accumulated damage model:

$$D = \int_0^{\varepsilon_p} \frac{d\varepsilon_p}{\bar{\varepsilon}_f} \quad (2.15)$$

where ε_p and $\bar{\varepsilon}_f$ are plastic and critical fracture strain, respectively. The accumulated damage model assumes that the fracture will occur when the accumulated damage (D) reaches the unity. The critical fracture strain $\bar{\varepsilon}_f$ can be considered as a function of the only stress triaxiality η (Golovashchenko, Hu, Choi, & Sun, 2014) in-plane strain condition as this one, in which the shear ratio is constant or linearly related with triaxiality (Hooputra *et al.*, 2004), while shear factor (Xue *et al.*, 2005) and Lode are considered equal to zero (Bai *et al.*, 2008).

Accepting the above-mentioned assumption and assuming a linear strain path for the material elements, it is possible to use the Rice-Tracey model (Rice *et al.*, 1969) expressing the plastic strain at failure as a function of the triaxiality state:

$$\bar{\varepsilon}_f = Ae^{-B\eta} \quad (2.16)$$

where A and B are the Rice-Tracey parameters that characterize the material model and depend on the grain size that can be computed considering different triaxiality states.

2.9 Heat treatment

Heat treatments are widely used in manufacturing in order to alter the properties, both mechanical and physical, of metals. They are essential processes in metal manufacturing that increase desirable characteristics of metal while allowing for further processing to take place (Konieczny & Henderson, 2007).

Considering the various aluminum alloys, only the 2xxx, 6xxx, 7xxx series go into solution to an appreciable degree presenting an appreciable precipitation hardening; these alloys are particularly suitable to solution heat treatments because of their chemical composition the main elements that precipitate in these aluminum alloys are copper in 2xxx series, magnesium combined with silicon (Mg_2Si) in 6xxx series, and zinc in the 7xxx series.

In a standard solution heat treatment (Figure 13), the material is held at high temperature to allow the elements to go into solution, the time and temperature differ for every material. Then the material is subjected to a rapid quench (generally in water) in order to preserve the solutioned structure at lower temperatures. The quench phase is followed by either natural aging (i.e. at room temperature) or artificial aging (holding the material in a furnace at a moderately elevated temperature) for precipitation hardening (Kaufman, 2000).

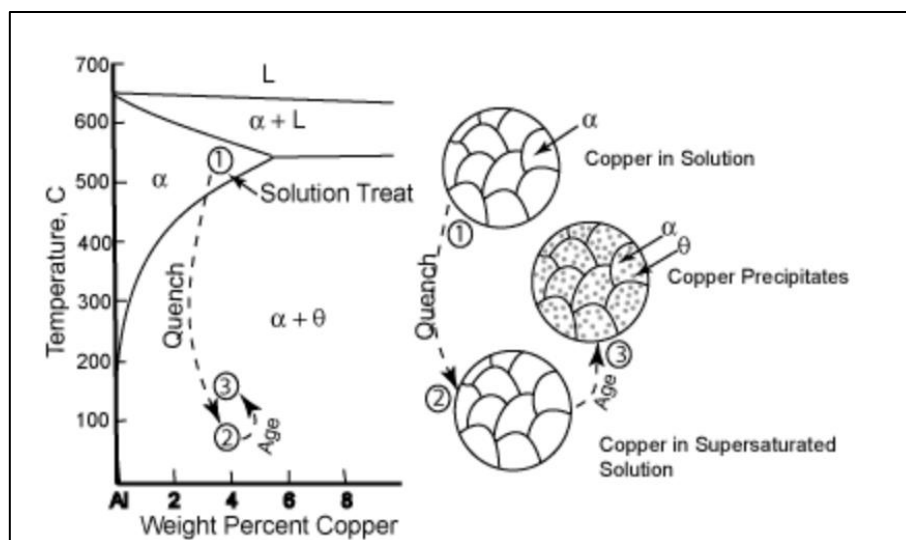


Figure 13 - Heat treatment of a 2xxx aluminum alloys in which are present the three main phases of the process: 1) solution treatment, 2) quench, 3) aging (Source: [NDT Resource Center](#)).

During the last decades, intensive research activity has focused on accumulating knowledge about the atomic and crystallographic structural changes that occur in supersaturated solid solution (i.e. aluminum alloys) during precipitation phase and how they affect the macroscopic mechanical properties of the material. In most precipitation-hardenable materials, a complex sequence of changes depends on time and temperature are involved.

One of the main variables is the kinetic of solution and precipitation. It indicates the relative rate at which a solution and precipitation reactions occur with different solutes depend upon the respective diffusion rates, in addition to solubilities and alloy contents. Diffusion coefficients for several alloying elements in aluminum were determined experimentally (Kaufman, 2000).

Another important variable of the solution and precipitation process is the nucleation. It indicates the formation of zones in which the solute elements can precipitate. Recently has been proved that a critical vacancy concentration is required for this process to happen and that discontinuities in the lattice greatly influence too. In fact, nucleation processes of new precipitates generally happen in the locations with the higher energy and greater disorder; in polycrystalline alloys, these locations are grain boundaries, sub-grain boundaries, dislocations, and interphase boundaries.

Quenching is in many ways the most critical step in the sequence of heat-treating operations. The objective of quenching is to preserve as much as possible the solid solution formed during the solution heat-treating temperature, by rapidly cooling usually near room temperature.

After quenching, most of the heat treatable alloys exhibit age hardening at room temperature; the rate and extent of such hardening varying from one alloy to another. Microstructural changes are negligible in room-temperature aging since the hardening effects are attributable only to the formation of zone structure within the solid solution. Since the alloys are softer and more ductile immediately after quenching than after aging, straightening, or forming operations may be performed more easily in the immediate post-quenched condition.

On the other hand, with artificial aging, the effects of precipitation on mechanical properties are greatly accelerated and usually accentuated, by reheating the quenched

material in a range from 100 to 200°C for aluminum alloys. The effects are not entirely due to a changed reaction kinematic, in fact, the structural changes occurring at the elevated temperatures present several and remarkable differences from those occurring room temperature aging. These differences are reflected in the mechanical characteristics and some physical properties. A characteristic feature of elevated-temperature aging effects on tensile properties is that the increase in yield strength is more pronounced than the increase in tensile strength. Also ductility, measured as percentage elongation, decreases compared to the natural age condition. Thus, an alloy in the T6 temper has higher strength but lower ductility than the same alloy in the T4 temper (Kaufman, 2000).

2.9.1 Heat treatment AA6xxx

In AA6xxx series Al forms a quasi-binary section with the Mg₂Si phase of the magnesium-silicon system, which in turn provides an excellent precipitation-hardening capability; this results in modestly higher strengths than possible with non-heat-treatable alloys, combined with generally excellent corrosion resistance. Aluminum 6xxx series are among the easiest of aluminum alloys to extrude and are thus widely used for complex produced in this manner. In addition, they are readily joined by almost all commercial processes (Kaufman, 2000). Some natural aging begins immediately after solution heat treatment, so forming operations should be scheduled soon after the material is quenched.

For AA6013 solution heat treatment is performed at 570 °C (1060°F) for 30 minutes followed by cold water quench in order to obtain the W temper. Aging will then occur naturally at room temperature for the T4 temper, while an aging heat treatment is needed to reach the T6 temper. More in detail, T6 tempers are generally obtained with warming the solutioned material for 4 hours at 190 °C (375°F) followed by air cooling.

2.9.2 Heat treatment AA7xxx

7xxx aluminum alloys, especially when combined with copper and magnesium, provide the highest strengths of any commercial series. As a group, these alloys possess relatively poor atmospheric corrosion resistance compared with other aluminum alloys and in general, are less tough and more susceptible to stress-corrosion cracking under short-transverse stressing.

The heat-treatable 7xxx series is characterized by alloying with Zinc, this bond confers little solid-solution strengthening to aluminum, although the addition of magnesium and/or copper to the aluminum-zinc alloy, results in attractive compositions for heat-treating and age hardening.

For AA7075 solution heat treatment is performed at 462 - 482 °C (870 - 900 °F) for 2 hours followed by cold water quench in order to obtain the W temper. Aging will then occur naturally at room temperature for the T4 temper, while an aging heat treatment is needed to reach the T6 temper. More in detail, T6 tempers are generally obtained with warming the solutioned material for 24 hours at 121°C (225°F) followed by air cooling.

Looking more in detail what happens to the microstructure, immediately after quenching, spherical GP (Guinier–Preston) zones are formed. Within a day of natural aging, the high concentration of zinc in these zones helps the diffusion of magnesium through vacancies to form GP clusters with average zinc to magnesium ratio of 1:4. Continuing the aging process, the metastable transition precipitate η' appears, and finally, the equilibrium η phase is formed. The sequence of precipitates can be summed up as following (Banhart, 2016):



The GP zones are coherent, η' clusters are semi-coherent and η phase incoherent with the main matrix. These steps assume that each metastable product generates nuclei for the subsequent phase. However, there is a strong interdependence between quenching, aging, and the resulting metallurgical microstructure of precipitates. High quench rates produce a fine dispersion of GP zones, and so a more uniform distribution of η' phases is obtained during aging. At an aging temperature up to 100°C both GP zones and η' clusters can be observed. The apparent solvus temperature for the formation of GP zones is approximately 135°C, so above 130°C up to 150 °C, GP zones rapidly dissolve to produce η' , which appears to be the first precipitate. The η equilibrium phase eventually forms from η' clusters, and the alloy's performances decrease (Mackenzie, 2016). The addition of more than 1wt% of copper creates a subcategory of the Al-Zn-Mg system that has special characteristics. Copper dissolves in the precipitates in modifying their composition and stabilizing the η' phase, resulting in an increased over-aging resistance (Banhart, 2016).

2.10 Lubricants

Lubricants play a significant role in sheet metal forming. Introducing lubricants between the surfaces in contact generally provides a better stress/strain distribution due to the lower friction among them. In manufacturing operations, lubricants strongly affect the

drawability, the surface finishing, and the tool life. Considering the Hole Expansion Test, lubricants facilitate the sliding of the sheet metal over the punch surface, an important condition in the flat-top punch, in which friction conditions can influence the location of instability and the degree of nonlinearity in the strain path, but they do not affect the necking limit. It is important to note that plane strain is the weakest forming condition. Thus, localized necking occurs more easily under plane strain conditions.

3 OBJECTIVES OF THE WORK

In this chapter, the objectives of the work are briefly defined and presented:

- 1) Define a finite element model able to describe the Hole Expansion Test of AA7075-T6 both at room temperature and warm conditions
- 2) Define a finite element model able to describe the HET for AA7075-T6 both with the conical and the flat punch expansion
- 3) Perform preliminary simulation of the hole expansion test and predict the HER with the available fracture criteria
- 4) Evaluate which parameters most affect the final Hole Expansion Ratio

4 FINITE ELEMENT SIMULATION

This chapter outlines the Finite Element simulation effort carried out. Section 5.1 presents a general description of the real manufacturing process, introducing the main variables and parameters that mostly affect the simulation results. Section 5.2 briefly presents the purpose of the simulation. In Section 5.3 a detailed description of the model is presented, in which all the design choices are motivated in agreement with the purposes of the simulation; this includes the material characterization for the various test configurations and the description of the applied boundary conditions.

4.1 Description of the actual forming process being modelled

Due to Covid-19 Pandemic, it has not been possible to carry out the experimental work. The scheduled experimental activity would have been focused on a wide-ranging characterization of the shear-edge sensitivity through HET of AA6013 and AA7075 in the under-age and peak edge conditions, including the evaluation of the effects on the HER of the various hole introduction techniques into the workpiece, as “drill and ream” or punching. Consequently to the aforementioned limitations, the work has focused on a modeling effort aimed to describe the hole expansion process for AA7075 in the T6 temper; the hole introduction techniques were not included in the model due to the leakage of experimental data.

The Hole Expansion Test (HET) can be modeled as a forming process in which the workpiece is clamped by the binder against the die, and the hole, present at the center of the blank, is expanded by a punch. The force exerted by the binder must be sufficiently high to prevent any material draw-in from the clamping area during the test.

All the elements present in this finite element simulation were modeled with SolidWorks®, meshed with HyperMesh™, and then implemented in LS-DYNA®. In this FEM simulation, two different punch geometries are considered: a 60° conical punch as prescribed by ISO-16630:2017 and a flat-bottom punch.

The circular geometry of the process allows exploiting the symmetries considering only a quarter of the complete one, as represented in Figure 14, thus reducing significantly the computational time.

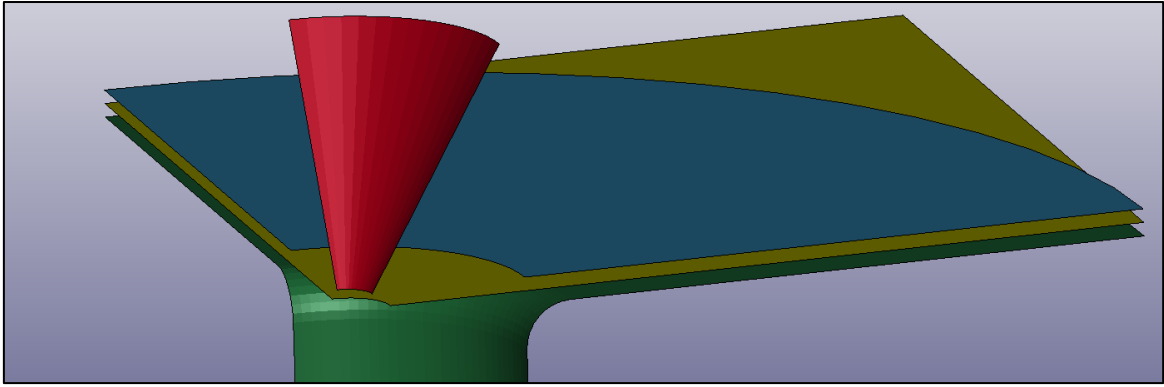


Figure 14 – Quarter model used for the simulation

4.2 Purpose of the simulation

This FE simulation aims to describe the deformation process in the Hole Expansion Test under the effect of various punch geometries.

Also, the execution of the test under warm forming conditions at 200°C will be simulated.

The strain states consequent to the various test configuration will be analyzed and compared and will provide a solid base of comparison with the experimental data.

The principal motivation for developing a Finite Element constitutive model of the Hole Expansion Test is the possibility to obtain a prevision of the experimental results saving time and costs.

4.3 Model description

4.3.1 Modelling approach

Because of the nonlinearities such as curved geometry, contact, and considerable plastic deformation, a dynamic explicit mechanical solver was selected for all the test configurations.

A coupled thermo-mechanical simulation was performed within LS-DYNA for the warm test configurations in which the blank is assigned an elastic viscoplastic material as described in Section 5.3.3. For the thermal solver a fully implicit solution algorithm with a diagonal scaling conjugate iterative solver and a flexible time step, that was restricted to a maximum temperature change of 25°C, was selected.

4.3.2 Geometry and Element type selection and rationale

The main dimensions of the model are coherent with the ISO-16630:2017, the tool clamping die (binder) has an opening diameter of 75 mm with a corner radius of 5 mm ; both the two punches have a base diameter of 50 mm and the flat one presents a fillet radius of 9 mm as reported in Figure 15.

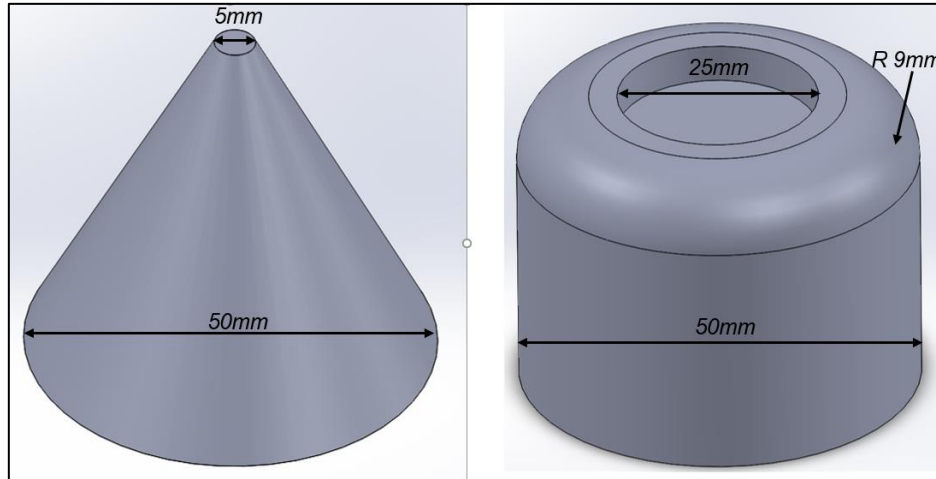


Figure 15 - Detail of the punch geometries used in the simulation

Workpiece, punches, binder, and die were modeled with four-node shell elements (Belytschko-Tsay formulation).

A quarter of the workpiece, a 177.8 mm (7 in) square blank with a 10 mm hole in the center, has been modeled with 3936 elements of different dimensions. The mesh design of the workpiece is composed by three regions: an internal region including the area up to 25 mm around the hole, an intermediate region including the area up to 70 mm from the hole, and an external region which includes the external part of the blank not covered by the previous regions. The inner and the intermediate areas have the same general mesh pattern, with 36 elements in the circumferential direction of 0.5 mm and 1 mm length along radial direction respectively; the external region presents a relatively coarse mesh. This mesh design choice is justified by the assumption that no significant strain and stress state will be present there as it is very far from the hole and punch action. The considered blank has a thickness of 2 mm and 7 integration points are present through the thickness.

In Figure 16 is represented a detail of the blank mesh in which the various mesh regions are highlighted.

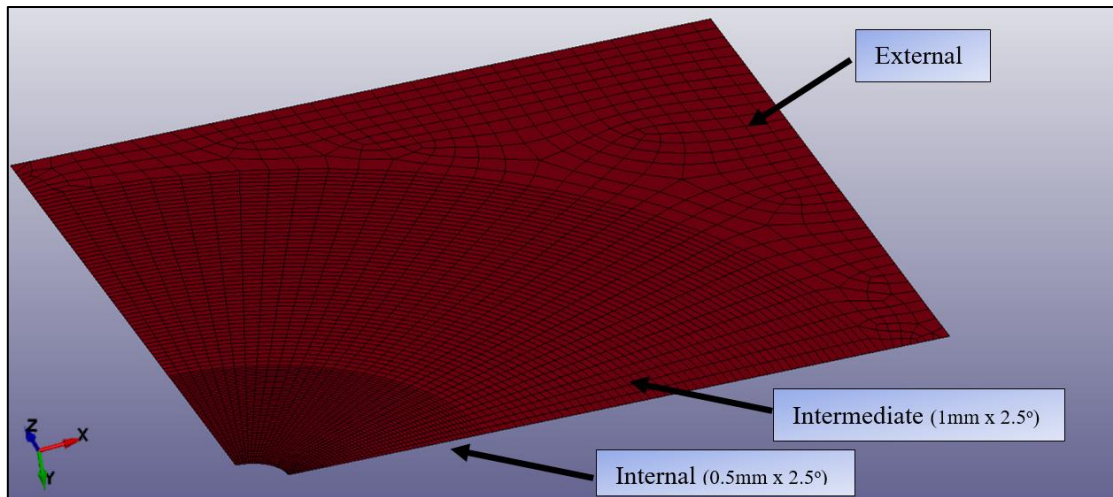


Figure 16- Detail of the workpiece mesh with a highlight on the three zones

The other parts of the assembly (Punch, Binder, and Die) were modeled with 4-node Belytschko-Tsay shell elements with an assigned thickness of 1 mm . For these parts, the mesh has a variable dimension. The binder and the die have the same radial mesh pattern. More in detail, the increment of element division was 6° in the circumferential direction and 1 mm in the radial direction for the binder, and 3° and 5 mm respectively for the die.

The conical punch has 6° element division along the circumference and 1.33 mm along the radial direction while the flat punch has 4.5° circumferential element increment 2 mm each along the radial direction.

Since these parts cannot be deformed, a larger mesh dimension has been used to model them since no strain will be recorded.

4.3.3 Material model adopted

The tooling parts (punch, binder, die) had been assigned the properties of steel with a rigid material type model. When the rigid material is assigned, the software does not compute any stress or strain of the parts, assuming them equal to zero. Even if this behavior may look like an unrealistic one, it is a good approximation for these kind of processes in which the tool deformation can be neglected compared to the blank one.

The material properties of the tools are reported in Table 3:

ρ [ton/mm ³]	E [MPa]	ν
7.88 e-09	208800	0.3

Table 3 - Material properties of steels assigned to the tools.

The blank sheet was assigned the mechanical properties of AA7075-T6 defined in Table 4 according to the room temperature characterization effort conducted by Rahmaan *et al.* (2016) that defined the constitutive response of AA7075-T6 sheet in tensile and shear loading. The considered material showed a mild strain rate sensitivity and a quite low anisotropy response, although a significant plastic anisotropy was measured in terms of Lankford coefficients.

The associative yield function Yld2000-2d proposed by Barlat *et al.* (2003) is used with the same calibration proposed by Rahmaan *et al.* (2016) and reported in Table 5. This Barlat model is ideal for sheet forming operations with anisotropic materials under plane stress condition and is present as a built-in function in LS-DYNA. The associative flow rule assumes that plastic potential and the yield function are the same function (Figure 17), hence one common set of calibrated anisotropy coefficient is sufficient to determine the model. The blank rolling direction is assumed to be along the x-axis.

Table 4 - AA7075-T6 Mechanical properties used in the simulation at 25°C (Rahmaan *et al.*, 2016).

ρ [ton/mm ³]	E [MPa]	ν	Yield [MPa]	UTS [MPa]	R_{00}	R_{45}	R_{90}
2.7 e-09	71700	0.33	504	572	0.78	0.95	1.34

Table 5 - Yld2000-2d parameters (Equation 2.20) for AA7075-T6 sheets proposed by Rahmaan *et al.* (2016).

Alloy	Parameters								
	α_1	α_2	α_3	α_4	α_5	α_6	α_7	α_8	m
AA7075-T6	0.89	1.09	1.97	0.42	0.47	1.93	0.99	1.08	8

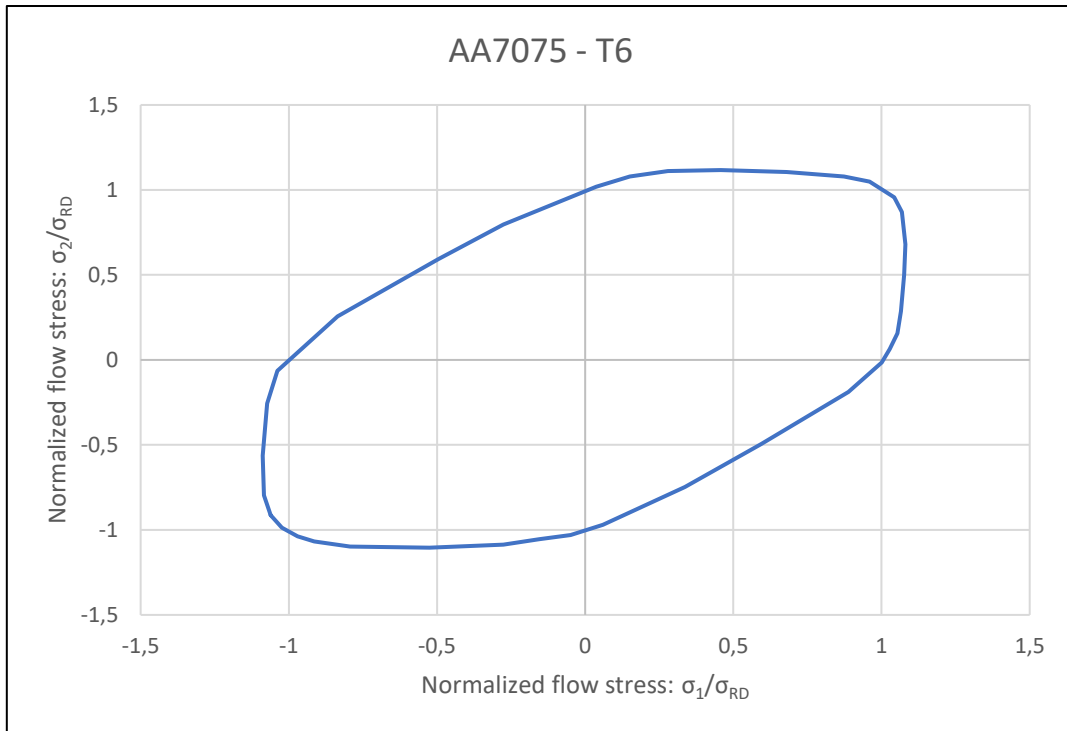


Figure 17 - Predicted Barlat YLD2000 yield surface for AA7075 – T6 sheet at plastic logarithmic strains of 0.08 in tensile test in the rolling direction (Rahmaan *et al.*, 2016)

The flow-stress curve was derived by the work proposed by Rahmaan *et al.* (2016), in which the tensile performance of the material is measure until the fracture of the sample (approximately at 0.1 of equivalent strain), then extended with a plastic work analysis, in which the measured shear-strain load is converted to uniaxial tensile values using von Mises criterion with the assumption of planar isotropy. The shear-data conversion was performed until strain up to 0.3 in order to stay within the infinitesimal strain range. These data are then fitted with a Voce hardening function for large strains as reported in Figure 18.

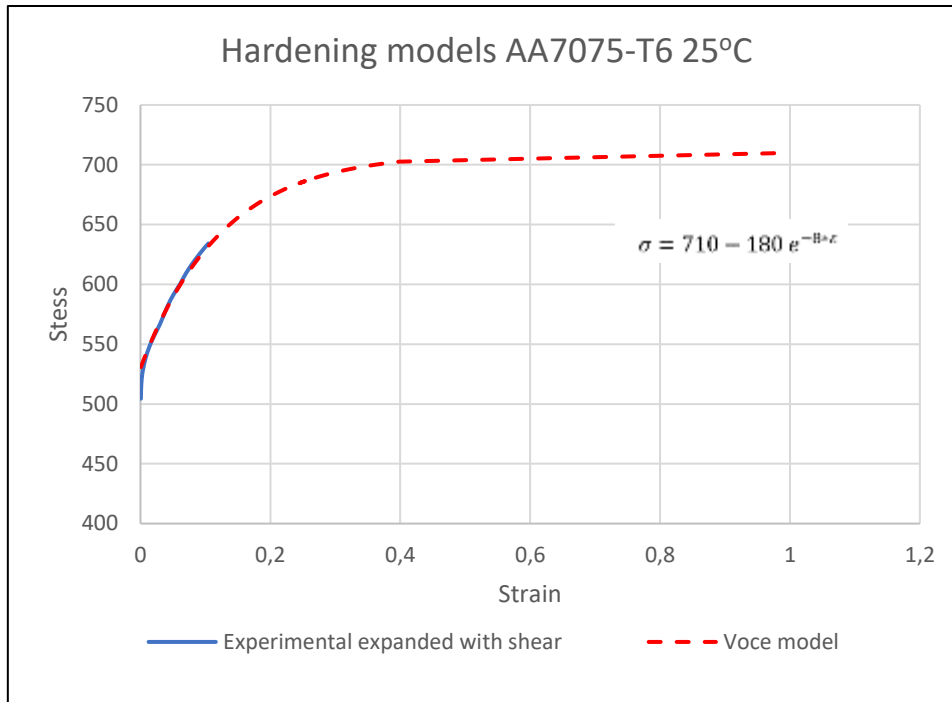


Figure 18 - Flow stress of AA7075-T6 along rolling direction at 25°C used in the simulation. Experimental data from Rahmaan *et al.* (2016)

The density of the material in the simulation is assumed 10^6 times larger than the original one, this technique is called “mass scaling” and it is often invoked to enable the models to run faster. Results are not affected since the inertia forces, in this case, are negligible.

The thermal response of the blank is computed through an isotropic material model. The tools are assigned an isotropic rigid material with properties of standard steel, for which neither strains nor stresses are computed with the intention of enhancing computational efficiency. Blank and tools thermal material properties are reported in Table 6.

Table 6 - Thermal material properties assigned to the tooling and the blank in the FE model (Source: Thermtest.com)

	Blank (AA7075 - T6)	Tooling (Steel)
Heat capacity	$9.6 * 10^2$ J/kg K	$4.6 * 10^2$ J/kg K
Thermal conductivity	200 W/m K	71 W/m K
Coefficient of linear thermal expansion	$2.3 * 10^6$ m/m K	-

The simulations in warm conditions were carried out considering two consecutive steps: in the first step, the material is assigned an isotropic elastic viscoplastic with thermal effect behavior, and in the second one it is used the Yld2000-2d yield function defined by Rahmaan *et al.* (2016) with the coefficients reported in Table 5, with a flow curve fitted on the elevated temperature stress-strain relationships proposed by Wang *et al.*

(2012) reported in Figure 10, and the material thermal properties present in Table 6 from the thermtest.com database.

In the first step, a thermal-mechanical simulation is carried out, in which the blank is warmed by the contact with the hot die and binder. The elastic viscoplastic model present in LS-DYNA allows considering the thermal effects of the material, receiving a table as an input containing a set of uniaxial stress-strain curves measured at various temperatures in order to have a different stress-strain response according to the local temperature of each element (Figure 19). This card also allows the defining of the other material parameters (*e.g.* Young's modulus, Poisson's ratio, yield stress) as function of the temperature.

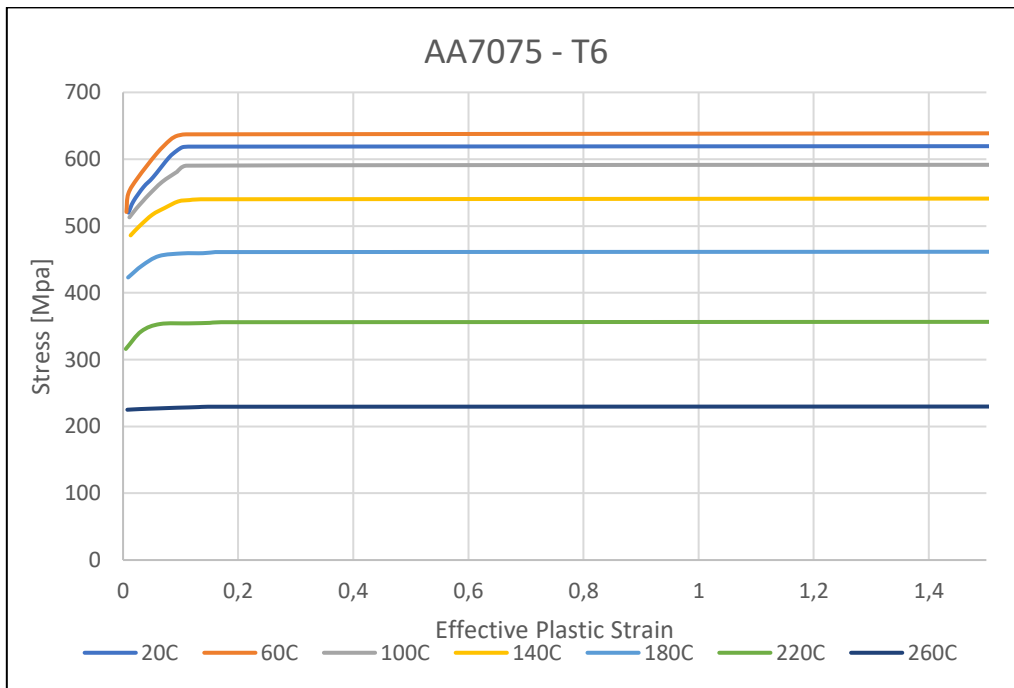


Figure 19 - Set of stress-strain relations used in the thermal-mechanical FE model based on Wang *et al.* (2012) data reported in Figure 10.

In the second step, the same Barlat Yld2000-2d yield function used for the room temperature test case is assigned with a strain hardening curve of the AA7075-T6 measured at 200°C by Wang *et al.* (2012) and fitted with the Voce hardening model (Eq. 2.7) as follow:

$$\sigma_f(\text{MPa}) = 409 - 31 * e^{-32\varepsilon_p} . \quad (5.1)$$

The first step of the warm simulation is useful to demonstrate that the gradient in the workpiece can be considered constant over all its surface after a transient and to evaluate the stress present in the material due to the temperature. Assuming that the workpiece has the same temperature of the tools, results in a simple mechanical analysis instead of a coupled thermal-mechanical one, and consequently in a faster simulation.

4.3.4 Boundary conditions

As already mentioned in the previous paragraphs, in order to save computational time and resources, a quarter symmetry condition is considered for the parts of the system.

This simplification implies the need to define additional boundary conditions in the system. The symmetry boundary conditions related to deformation, are applied only on the blank since it is the only deformable part. More in detail, all the nodes that lie on the symmetry planes have constrained some displacement and rotation as shown in Figure 20 to maintain the behavior of the full blank.

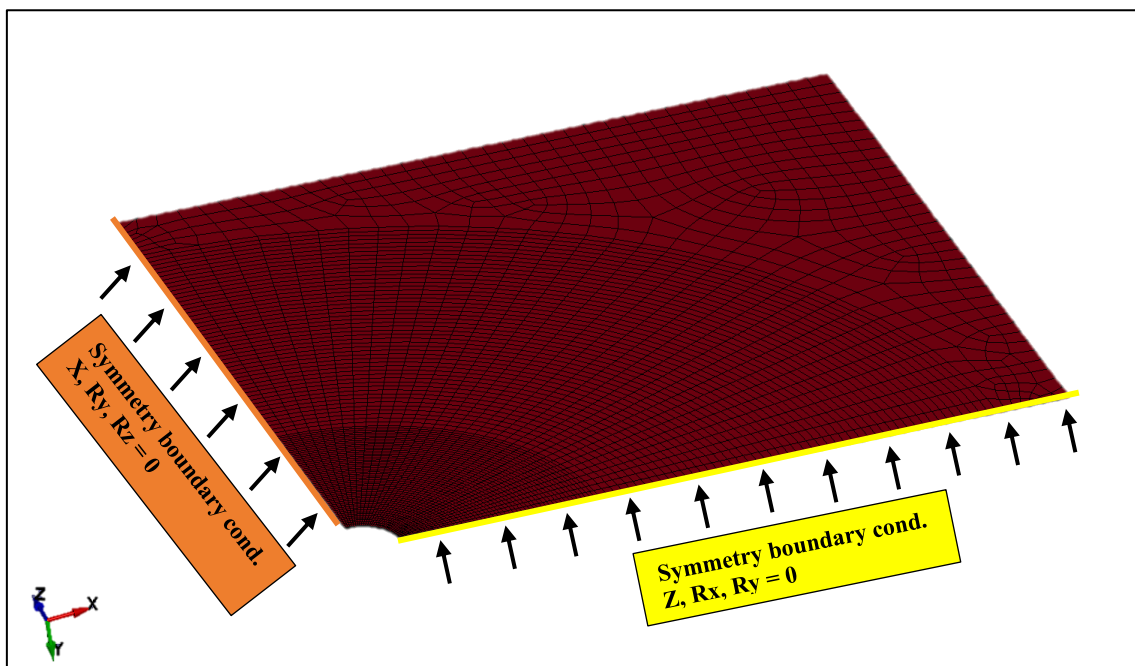


Figure 20 - Detail of symmetry boundary conditions applied on the workpiece

Except for the already mentioned edges on symmetry planes, the blank sheet is essentially free since the aim of the process is to deform it.

Due to the lack of experimental data, the effects of hole piercing on the blank was neglected. In other words, the detailed shearing process was not modeled.

The contact of the workpiece with the binder and die is considered as bare metal vs metal contact (unlubricated), the static and dynamic friction coefficients are set as $f_0 = 0.2$ and $f_d = 0.2$ respectively, while between the punch and blank a Teflon™ sheet was considered as a lubricant, and consequently, the friction coefficients are set as $f_0 = 0.04$ and $f_d = 0.04$.

Punch movement starts after one second of simulation time and is controlled by the sinusoidal loading curve (Figure 21) that imposes a constant speed of 1 mm/s as prescribed by the ISO16630. Using boundary conditions, the movement of the punch is limited to vertical displacement along the y-axis.

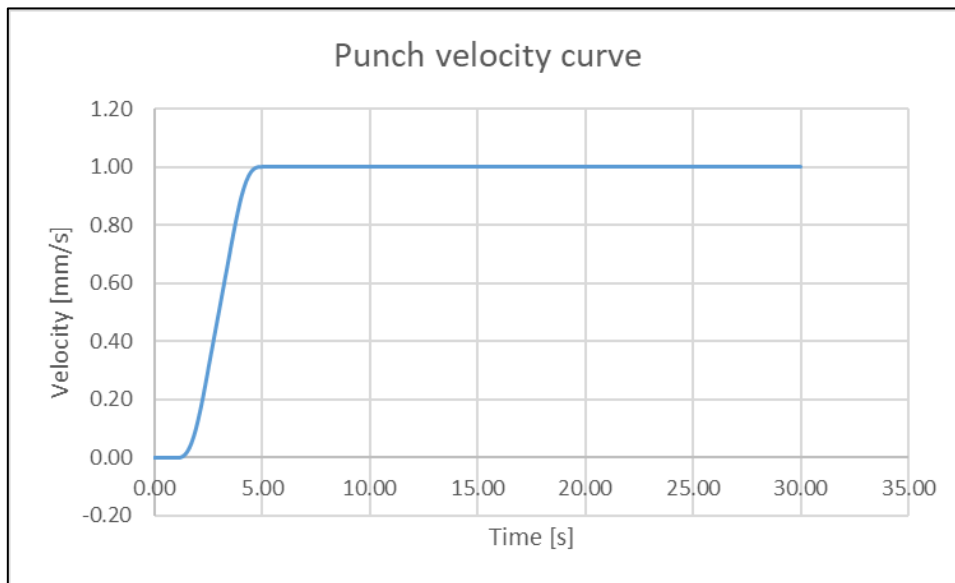


Figure 21- Punch displacement vs time

The Binder clamps the blank sheet with the die with a force of 70 kN, the quarter model applies only one-quarter of the total load (17.5 kN). It can move only along the vertical axis until $t = 1\text{ s}$ and with maximum a speed of 3 mm/s, then its movement is constrained, as shown in the velocity function of Figure 22. The displacement constrain curve of the binder is defined according to the consideration that the punch starts its movement at $t = 1\text{ s}$, and so the binder has one second to clamp the workpiece against the die (binder to die distance is set to 3 mm).

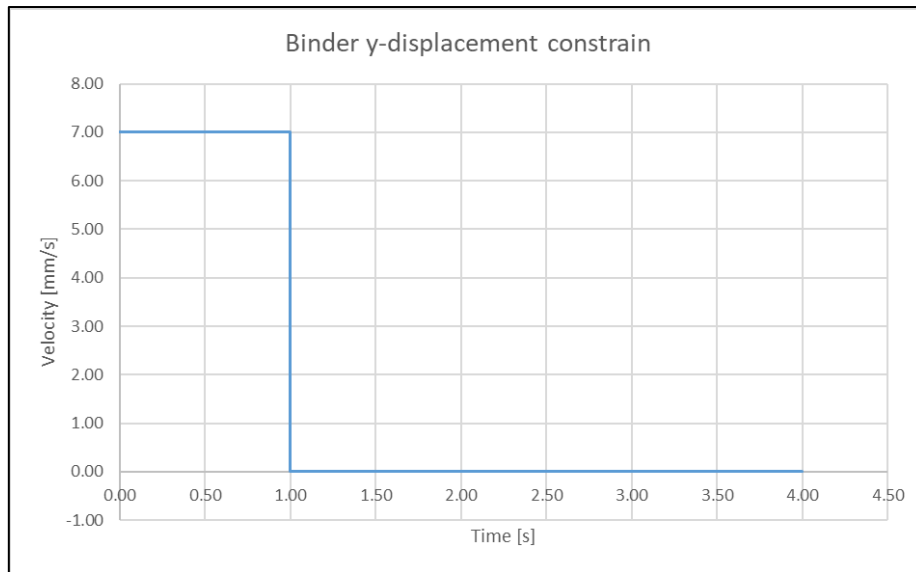


Figure 22 - Binder displacement vs time

The die motion is constrained both on axis-displacement and rotations. In the warm condition simulation, the binder, die, and punch are assigned a constant temperature of 200°C through a prescribed thermal boundary condition, while the workpiece is assigned 25°C as initial temperature. A one-way thermo-mechanical penalty-based contact algorithm was utilized between the blank and tooling.

5 RESULTS

In this chapter, the main results of the simulations are reported and commented on in all the various considered configurations.

Since failure criteria were not considered in the simulation model, in order to detect the moment of the failure (not the position!) Stress based FLD were used as failure criteria in the post-processing analysis, in a similar manner to the one proposed by Manikandan *et al.* (2016), mapping them from FLC in strain space to stress space. For this purpose, von Mises yield function, volume consistency, and associative flow rule are used. The use of von Mises function instead of that of Barlat results in a simplification that does not consider the material anisotropy behavior, although the anisotropy in stress response for this model is quite low (Ramhaan *et al.*, 2016); this solution was adopted because of the mathematical complexity in mapping the forming limit curves with the Barlat function (Eq. 2.15).

The forming limit curves of the AA7075-T6 at 25°C, 200°C, and 230 °C are reported in Figure 2. The forming limit stress curves (FLSC) are obtained considering the von Mises yield function for plane stress cases previously reported as Equation 2.14:

$$\sqrt{\sigma_1^2 + \sigma_2^2} - \sigma_1\sigma_2 - \sigma_f = 0, \quad (2.14)$$

then defining the ratio of the minor true strain ($d\varepsilon_2$) to the major true strain ($d\varepsilon_1$) by the parameter α :

$$\alpha = \frac{d\varepsilon_2}{d\varepsilon_1} \quad (6.1)$$

similarly, the ratio of the minor true stress (σ_2) to the major true stress (σ_1) is defined by the parameter β :

$$\beta = \frac{\sigma_2}{\sigma_1} \quad (6.2)$$

The two parameters α and β are related by the expressions:

$$\alpha = \frac{2\beta - 1}{2 - \beta} \quad (6.3)$$

$$\beta = \frac{1 + 2\alpha}{2 + \alpha} \quad (6.4)$$

Further, the equivalent plastic strain increment can be written as:

$$d\varepsilon_{eq} = \frac{2}{\sqrt{3}} d\varepsilon_1 \sqrt{1 + \alpha + \alpha^2} \quad (6.5)$$

The Voce function represented in Figure 18 is then used as a stress-strain relation with the same parameters, here reported:

$$\bar{\sigma}(MPa) = 710 - 180 e^{-8 \bar{\varepsilon}} \quad (6.6)$$

Once the effective stress $\bar{\sigma}$ values are obtained, it is possible to compute and plot the relation among σ_1 and σ_2 for an element, as reported in Figure 26 and Figure 27.

According to von Mises stress contours and the effective plastic strain distribution recorded during the simulation, the most critical points have been identified at the hole edge for the conical hole expansion (Figure 24). On the other hand, for the expansion with the flat-bottom punch, the von Mises stress and the equivalent plastic strain contours show that a wide area, covering the workpiece from the hole edge to the punch fillet, have an almost uniform stress values (Figure 25); in order to detect the first element that reaches the limit, several of them were recorded along the rolling direction (correspondent to the x-axis), the selected recorded points and their labels are represented in Figure 25a for the conical expansion model, and in Figure 25b for the flat one.

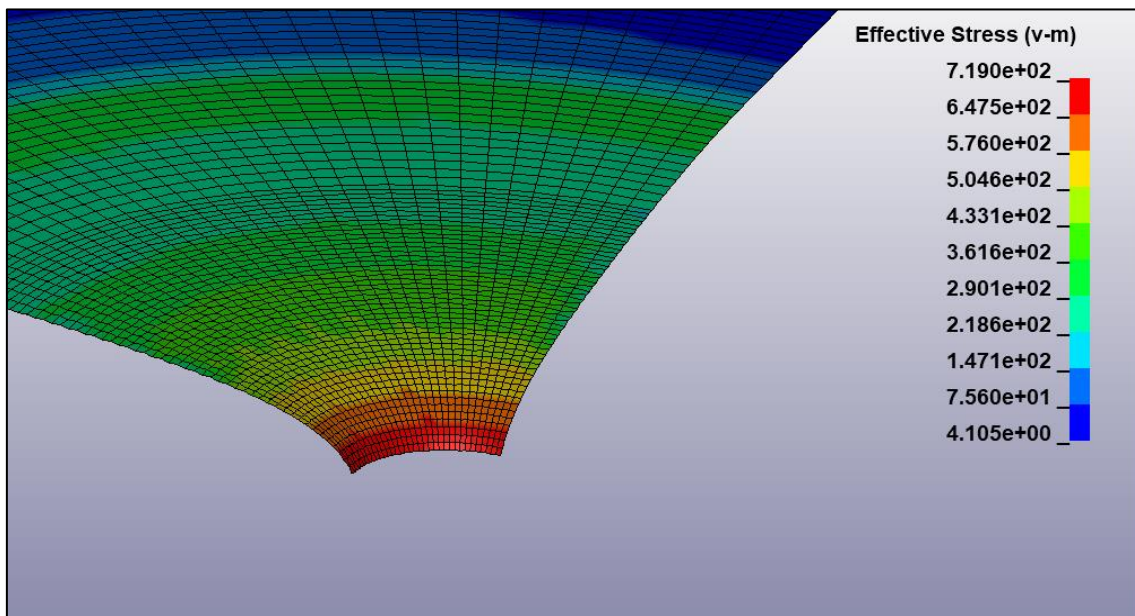


Figure 23 – Conical Hole Expansion simulation, effective stress (von-Mises) contour at the failure time according to FLSD

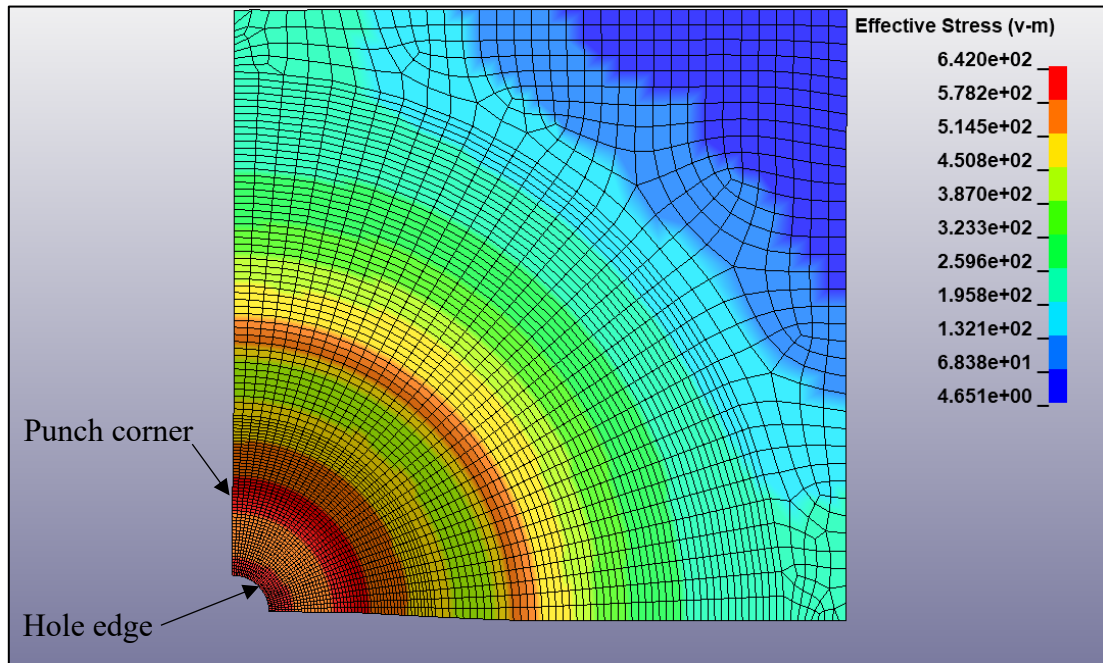


Figure 24 - Flat Hole Expansion simulation, effective stress contour at the failure time according to FLSD

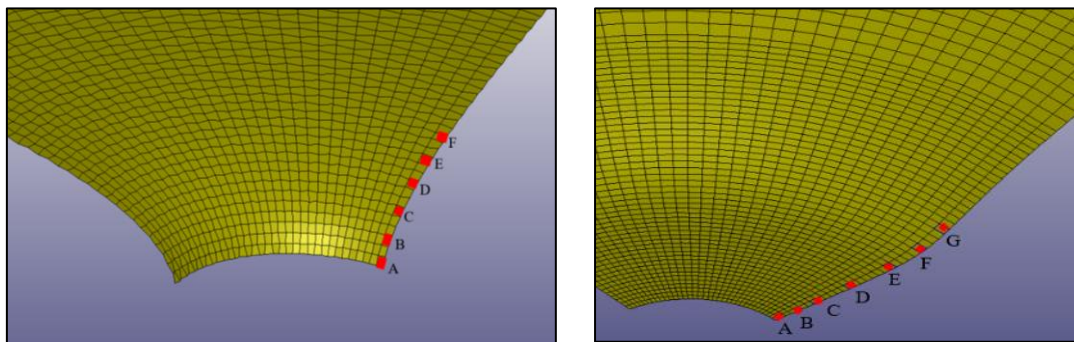


Figure 25 - Selected elements for the strain analysis along workpiece rolling direction. a) Point A and B location on the conical expansion blank. b) Point A to point G location on the flat expansion blank.

With reference to the selected elements of Figure 25, in Figure 26 is reported the evolution of the principal stresses of the most critical element on the hole edge during the conical expansion at 25°C; for the conical expansion, in Figure 26 is reported only the element on the edge since the stress decreases suddenly along the radial direction. For the flat expansion simulation at room temperature, the recorded in-plane principal stresses of the elements located from the hole edge to the punch corner along the rolling direction are

reported in Figure 26, where it is possible to see how the element B near the hole area ($l \div 3mm$ away from the hole) is the first element reach the FLSC than the others.

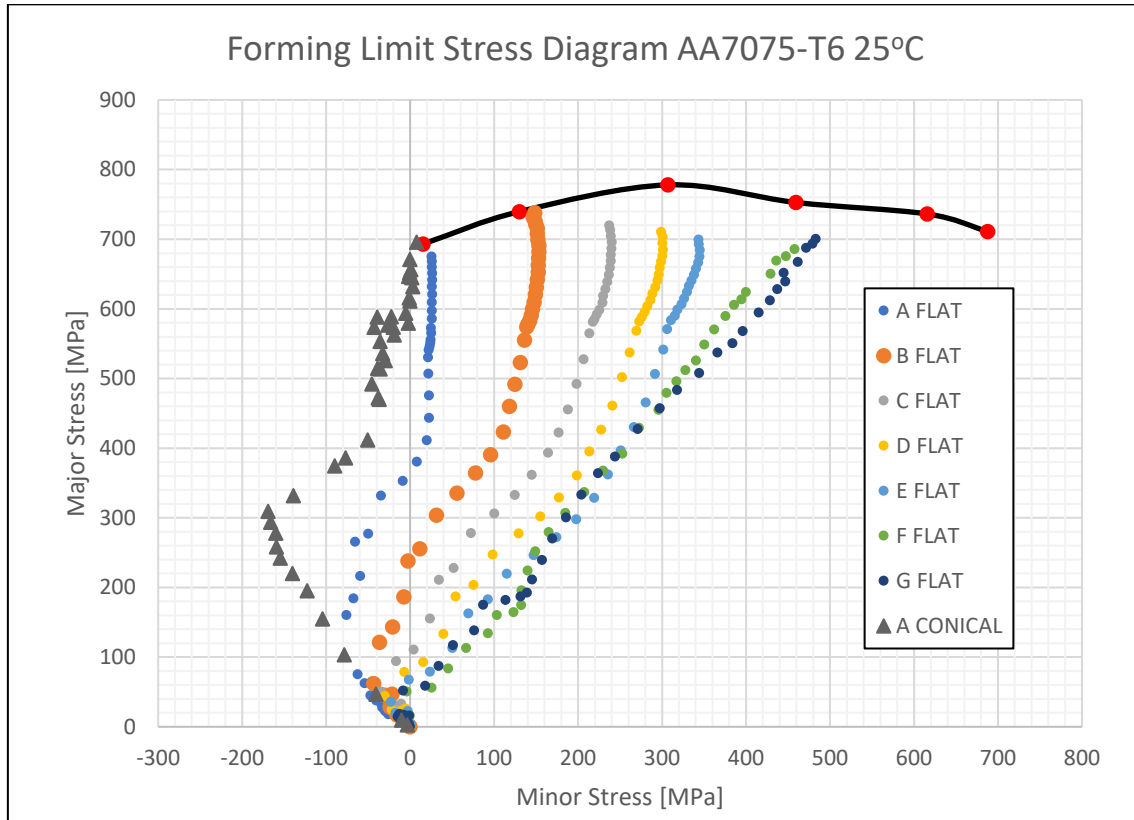


Figure 26 - Forming Limit Stress Curve AA7075-T6 at 25°C. In the conical expansion, the element on the edge is the first to reach the stress limit; in the flat expansion, the point B is the first. The element labels refer to Figure 25a and Figure 25b for the conical and flat case, respectively.

The same failure criterion is used to determine the forming limit of the simulations in warm conditions. The distribution of stresses and strains does not differ from the cases at room temperature except for the absolute values. As a consequence of this fact, also for warm condition simulations, the record elements have been taken from the hole edge in the conical expansion model, and from the hole edge to the punch fillet in the flat expansion. In Figure 27 the paths of the in-plane principal stresses of the elements present in these areas of the workpiece are reported.

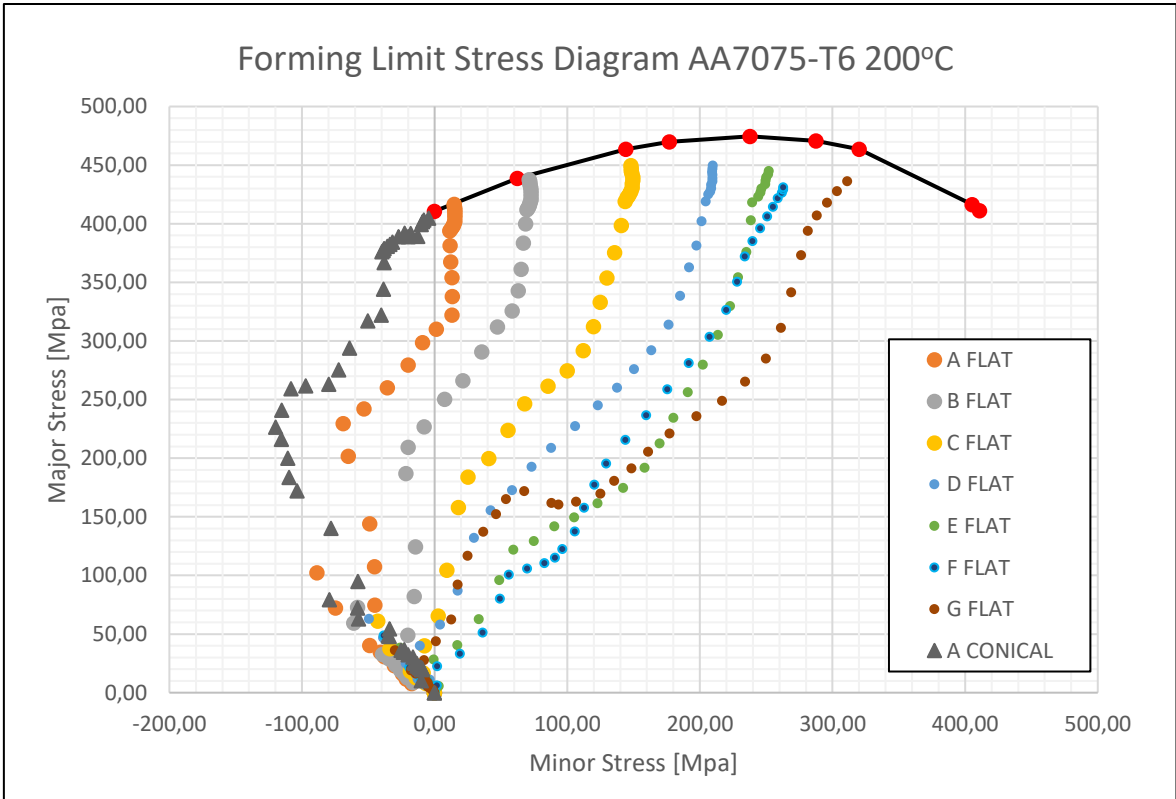


Figure 27 - Forming Limit Stress Curve AA7075-T6 at 200°C. The element labels refer to Figure 25a and 25b for the conical and flat case, respectively.

The corresponding Hole Expansion simulation results are reported in Table 7. As expected, and in agreement with the literature review, with the conical punch is possible to reach higher hole expansion ratios rather than with the flat-bottom one. Also, an increase in temperature results in a larger final hole expansion ratio for both the punch geometries.

Table 7 - Predicted Hole Expansion Ratio for conical and flat expansion at 25°C and 200°C

Hole Expansion Ratio	Conical	Flat
25°C	28.5	19.5
200°C	35.8	24.2

5.1 Room temperature hole expansion results

This paragraph will focus on the analysis of the workpiece stress-strain state at the time of the predicted failure in room temperature conditions.

5.1.1 In-plane strains

Considering the hole edge in the conical expansion, the deformation path of a single elements along the rolling direction is shown in the Figure 28. The deformation at the

edge follows a uniaxial strain path as expected. Moreover, from the hole edge (Point A in Figure 25a) to punch shoulder (Point F) stress varies from uniaxial to plane tension. Although generally, the plane state may be a more dangerous strain condition than the pure uniaxial, in the conical case equivalent stress/strain state presents at punch shoulder (point E and F) is very low compared to the one present at the edge as shown in Figure 28.

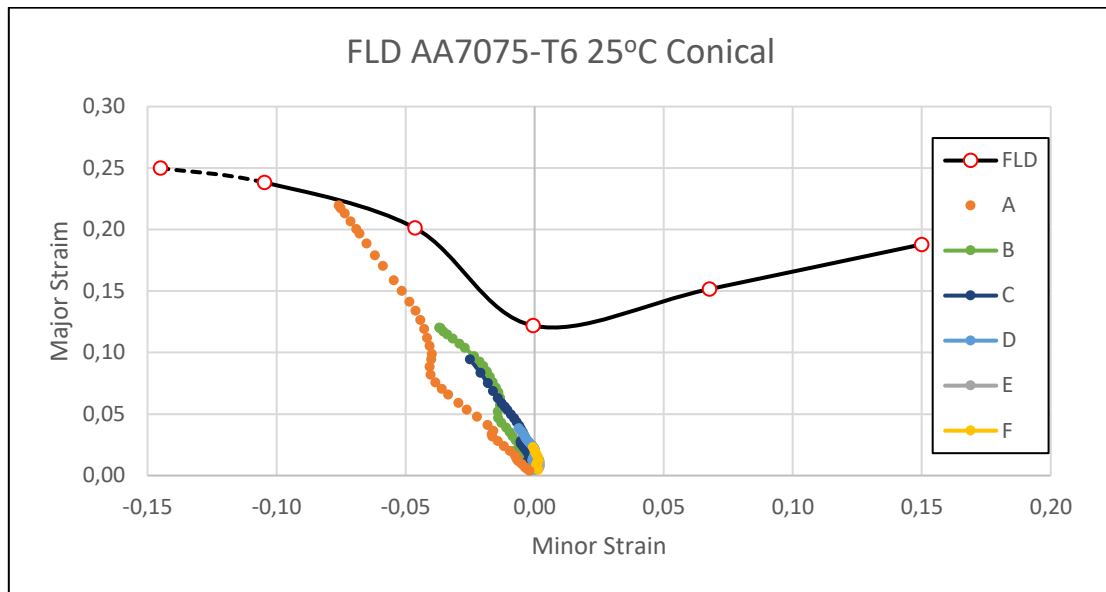


Figure 28 - Strain path of Conical Expansion, 25°C, at the hole edge (point A) and punch shoulder (point F). The element labels refer to Figure 25a (FLD source: Sotirov et al. (2012)).

On the other hand, the stress and strain state in the flat punch expansion case requires more complex analysis. As already mentioned, a wide area, from the hole edge to the punch shoulder, reaches the strain limit almost at the same moment. The stress present at the punch shoulder depends mostly on the configuration of the experiment, it can be decreased by the use of lubricants, that allow the metal sheet to “flow” over the fillet of the punch; another way to decrease the effect of the stress in that area is to adopt a larger corner radius of the punch.

Considering the elements along the rolling direction, for the flat case, it is possible to notice in Figure 29 how the strain paths are different from the hole edge (Point A in Figure 25b, pure uniaxial tension) to the punch shoulder (Point G in Figure 25b, biaxial stretching). Between these two areas, just next to the hole edge elements, it is present a plane-strain state (B and C point), that it is very close to the strain forming limit curve and might lead to the crack onset since this condition is the region in the strain plane where the forming limit curve has its minimum value.

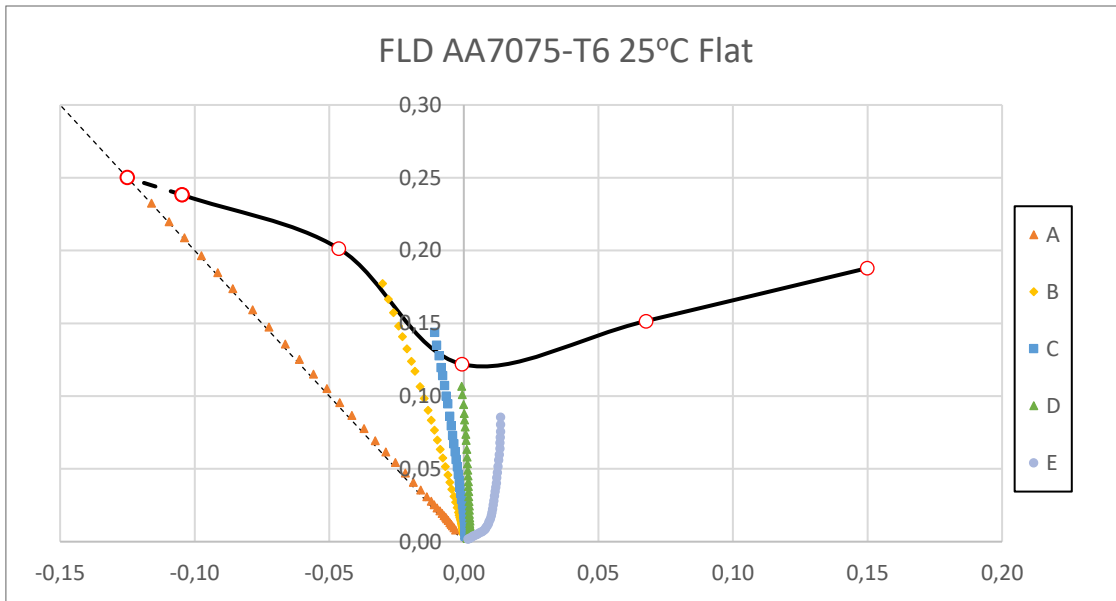


Figure 29 - Strain path of Flat Expansion, 25°C, from the hole edge (point A) to the punch shoulder (point G); (FLD source: Sotirov et al. (2012)).

5.1.2 Thickness strain distribution

Figure 30 shows the thickness reduction (absolute values of the thickness strain) measured along the rolling and transversal direction of the workpiece recorded during the simulations at 25°C. The horizontal axis represents the spatial radial coordinates of the strain measurement position measured from the hole edge.

The thickness strain profiles along the rolling direction and transversal direction follow the same trend, although the transversal direction looks less sensitive to thickness reduction.

The position of minimum thickness is located on the hole edge for the conical expansion, while it is approximately 2-3 mm away from the edge in the case of the flat expansion. These two areas are the most critical ones, where it is possible to identify the tendency to localized thinning.

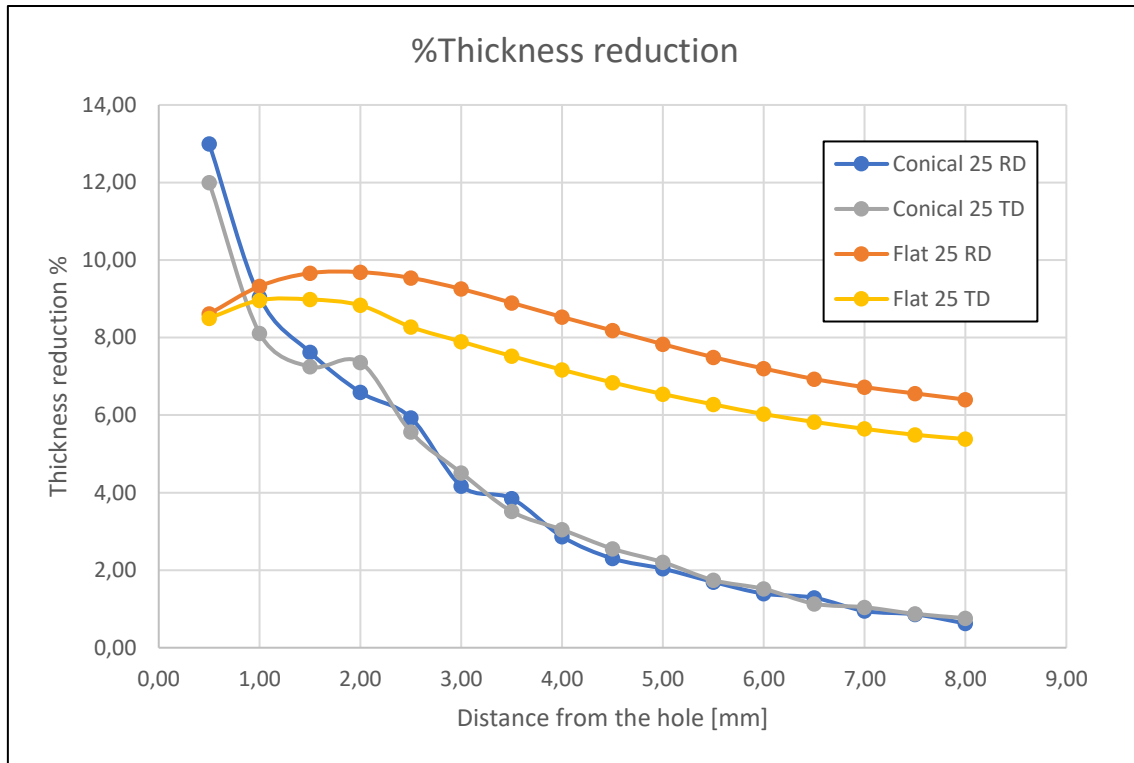


Figure 30 - Thickness reduction along the rolling direction from the hole edge up to 8mm, for both the conical and flat expansion workpieces.

5.1.3 Triaxiality distribution and MCC

A deeper analysis of the stress-strain state present within the workpiece can be done assessing the stress triaxiality in order to determine the fracture mode and also to compare it with the stress and strain limit previously presented in this work.

Figure 32 and Figure 33 show the distribution of stress triaxiality at the moment of the predicted failure in the conical and flat expansion respectively.

The hole edge in all the simulations presents a uniaxial state (0.33). Thus, it is reasonable to consider that deformation behavior during the HET is related with tensile deformation behavior of materials (low or negligible shear edge effects are assumed in the workpiece). This triaxiality result supports the approach to connect HER and tensile properties presented in previous literature studies (Paul, 2014; Konieczny & Henderson 1999).

In the conical expansion, the upper layers away from the edge present values typical of the biaxial tension (0.50÷0.66, red zone in Figure 32), but the internal layers of the elements present a very low (negative) triaxiality. This fact, in addition to the very low stress and strain state (compared to the one present at the edge), confirms that this zone can be considered safe from crack.

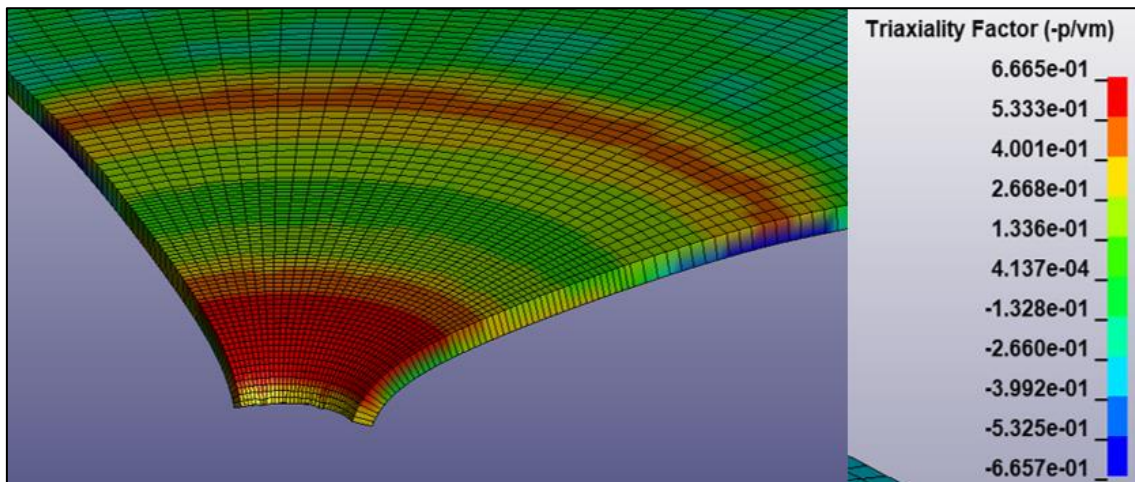


Figure 31-Contour of stress triaxiality within the workpiece on the conical expansion, 25°C.

On the contrary in the flat expansion, the elements in the proximity of the hole edge (the orange area in Figure 33) have triaxiality values in the range of plane-strain (approximately from 0.4 to 0.55), the most dangerous condition in FLD.

The elements in contact with the punch fillet show high triaxiality values in the range from 0.5 to 0.66; although this range, typical of biaxial tension, might represent a dangerous condition for the material, the measured equivalent strain in these elements (point labeled F and G in Figure 25b) is very low compared to those in contact with the flat zone of the punch, as shown in Figure 34.

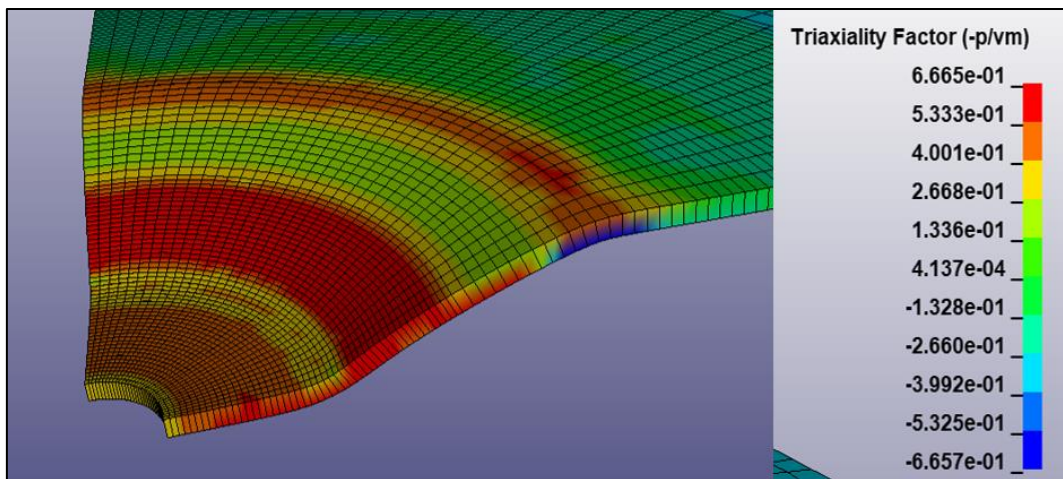


Figure 32 - Contour of stress triaxiality within the workpiece on the flat expansion, 25°C

The clamping zone between the blank and the die/binder presents negative triaxiality values, preventing a fracture in those areas. (Kacem, 2013). In sheet metal forming

processes, the area located in the vicinity of the die radius is generally favorable for crack initiation. Therefore, the die radius is one of the most sensitive parameters for all these processes (Kacem, 2013).

A phenomenological fracture locus such as the Modified Mohr-Coulomb (MMC) model can be used to investigate the fracture surface of materials relating the stress triaxiality vs the equivalent strain evolution. The calibration of the fracture locus (Rahmaan, 2020) is obtained by combining the fracture stains and triaxiality for a variety of samples with different shapes.

In Figure 33 and Figure 34 is present the MCC calibrated by Rahmaan (2020) and the triaxiality evolution versus effective strain of point A and B with reference to Figure 25a for the conical expansion. Again, the elements on the edge, as element A, are the ones that first reach the equivalent fracture strain.

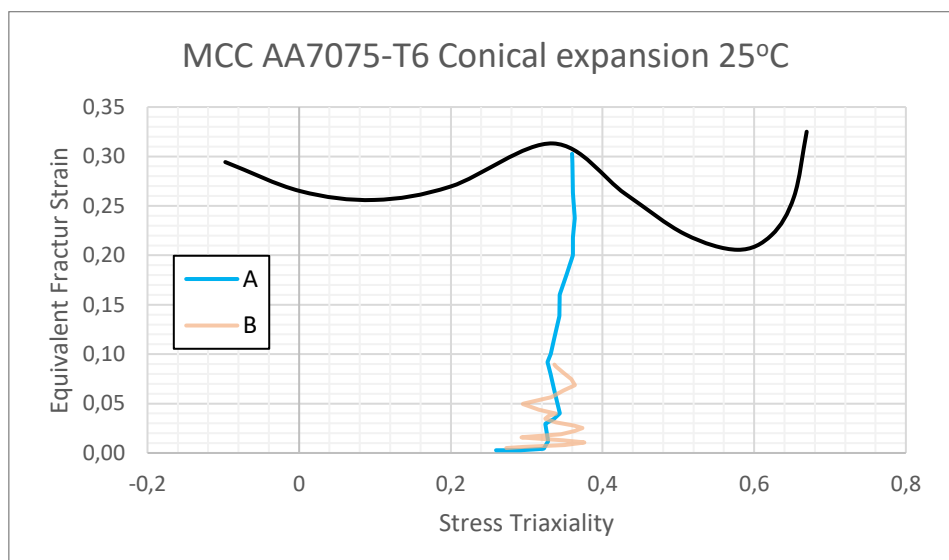


Figure 33 - MCC AA7075-T6 (Source: Rahmaan, 2020)

Figure 34 shows the equivalent strain vs triaxiality of the elements A, B, C, and G respectively (element labels refer to Figure 25b). It is immediate to notice that the B point is the first one to approach the fracture limit with a triaxiality value between the plane-stress and uniaxial. Although the elements in the plane region are the first to reach the limit curve, it must be considered that in the proposed simulation models is neglected the possibility of a loss of fracture strain limit due to edge shearing. In fact, the presence of a sheared edge, with the work-hardening due to the SAZ around the hole, would affect the accumulated stress on the element A more than for element B, as the effects of the SAZ decrease along the radial direction.

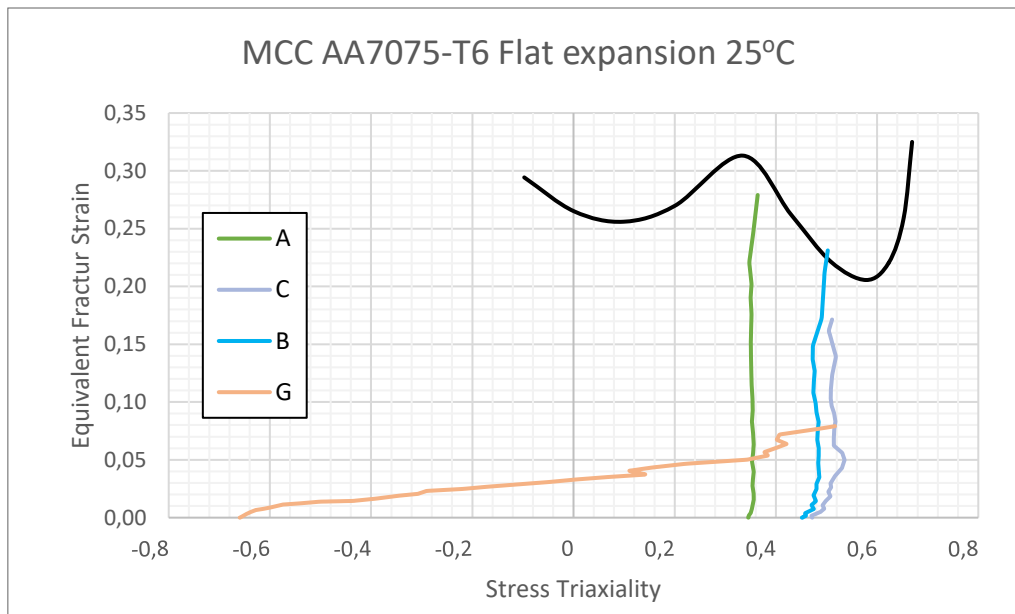


Figure 34 - MCC AA7075-T6 (Source: Rahman, 2020)

5.2 Warm Temperature Hole Expansion results

This paragraph will focus on the analysis of the workpiece stress-strain state at the time of the predicted failure in warm temperature conditions.

As explained in the previous chapter, the first part of the warm simulations was to run a model able to capture and describe the temperature evolution during the warming phase. In Figure 35 the temperature evolution of three different elements of the blank is reported until 180 seconds after the clamping against the warm binder and die; the position of the three elements and their labels refer to Figure 36, in which is also present the blank temperature distribution at 180 seconds after the beginning of the simulation.

The simulation confirms the presence of a temperature gradient within the blank after 180 seconds, with a recorded temperature difference from the clamped part to the hole edge, of approximately 20°C. The elements present in the clamped area (as element A), show a sharp increase in temperature once they enter in contact with the warm tools. On the contrary, elements B and C require more time than element A to warm up to the test temperature. This result agrees with the previous simulations and experimental results present in the literature (Noder, 2017). The relative small temperature gradient predicted within the blank allows, as a next step, the use of a simplified model for the hole expansion operation in which the temperature of the blank is constant and equal to 200 over its surface.

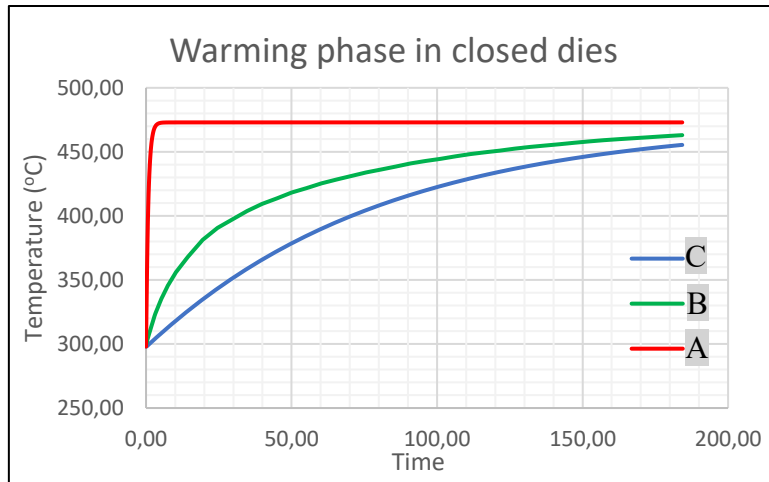


Figure 35 – Temperature evolution of elements A, B, C of the blank up to 180 seconds since the clamping. Element labels refer to Figure 36.

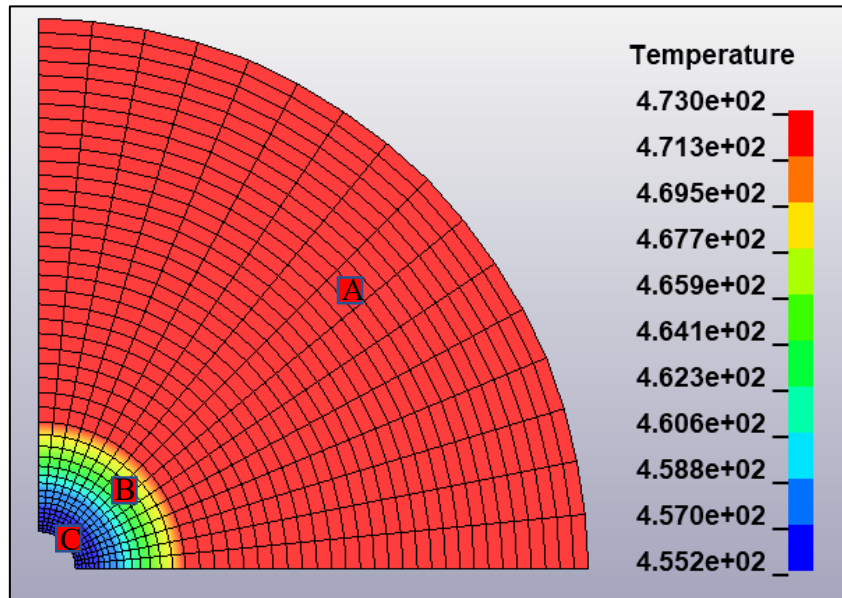


Figure 36 – Temperature gradient within the blank after 180 seconds since the clamping.

In Figure 37 is possible is shown the stress distribution within the blank due to the warming process. The stress values results are relatively low (within the elastic domain) and uniformly distributed along the blank surface.

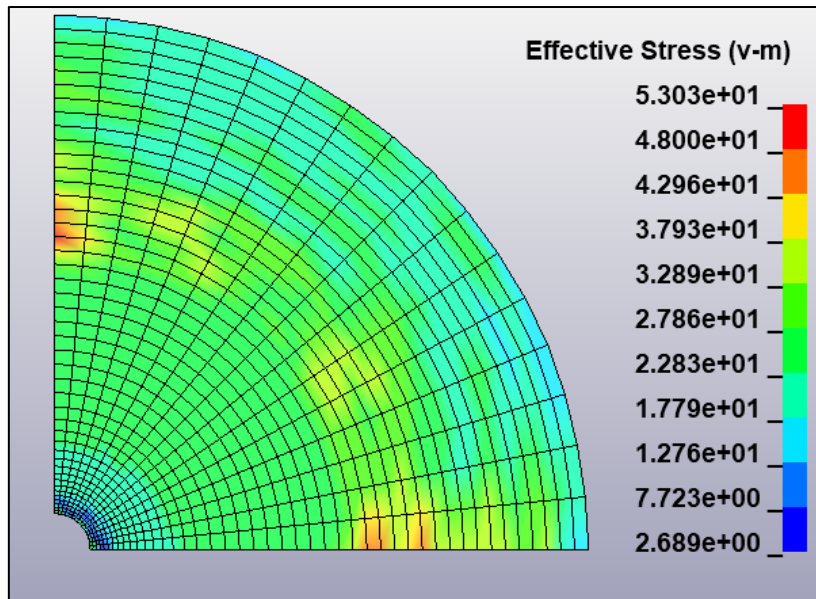


Figure 37- Thermal stress induced in the blank due to warming.

In the conical expansion at 200°C, the deformation path of a single element on the hole edge is shown in Figure 38. The deformation at the edge follows a uniaxial deformation path similar to what is shown in the case at room temperature. Moreover, from the hole edge (Point A in Figure 25a) to punch shoulder (Point F) deformation varies from uniaxial to plane-strain. The main difference with the room temperature case is that the area with high stress, with values close to the stress forming limits, is larger. This is mostly due to the increased material ductility, which allows the conical punch to penetrate more inside the workpiece respect to the room temperature simulations.

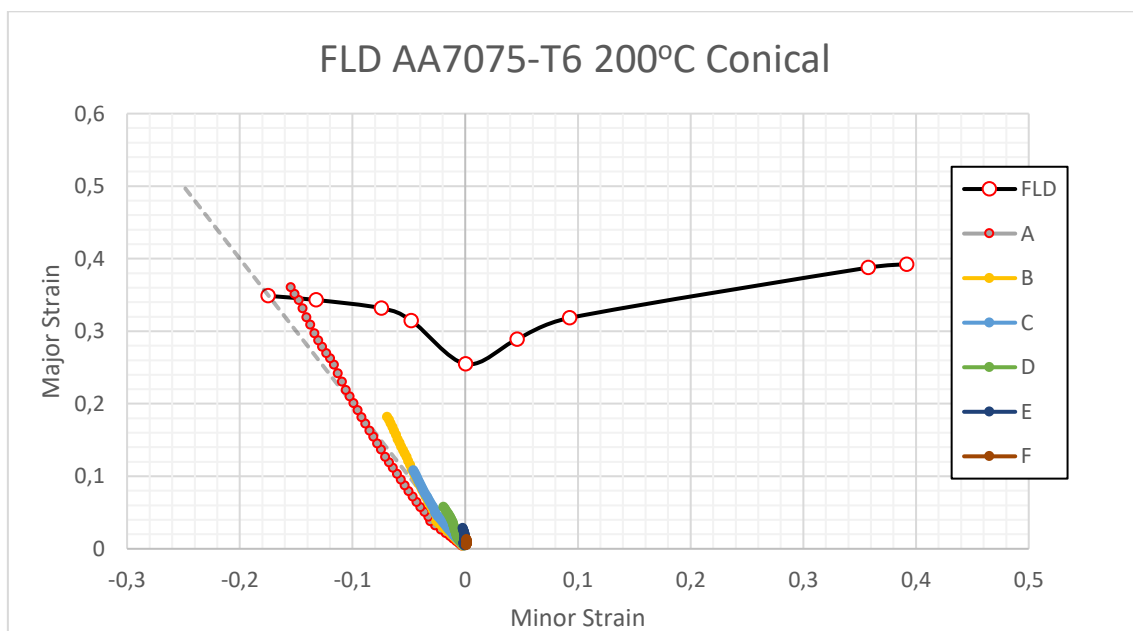


Figure 38 - Strain path of Conical Expansion, 200°C, from the hole edge (point A) to the punch shoulder (point F). The element labels refer to Figure 25a (FLD source: Sotirov et al. (2012)).

Nevertheless, the general trend of decreasing stress along the radius is confirmed also for the conical expansion in room temperature, it is therefore reasonable to assume that also in this case the fracture will occur on the hole edge in a tensile mode since the triaxiality values in this area are around 0.33 as shown in Figure 39, typical of uniaxial strain.

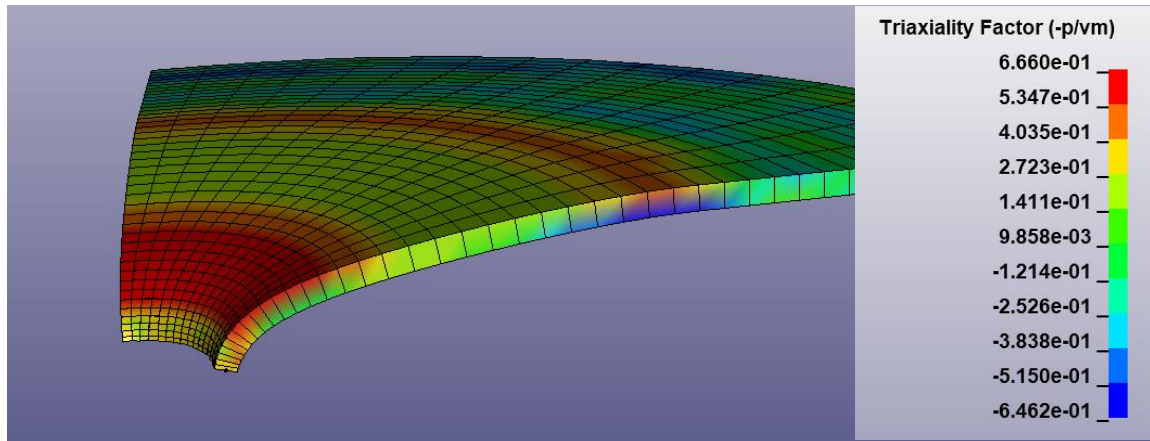


Figure 39 - Contour of stress triaxiality within the workpiece on the conical expansion, 200°C.

For the flat expansion simulation at elevated temperatures, the strains have similar behavior to the room temperature case. In Figure 40, is reported the major vs minor strain path of the element along the rolling direction labeled as showed in Figure 25b, in which the point A corresponds to the element in the hole edge and the point F (the last one) corresponds to the punch shoulder element. The edge presents a uniaxial deformation path (point A), bounded by an area that presents a plane-strain state with very high values (points B and C) in which crack should onset since they are the first to approach the forming limit, as reported in Figure 40. The elements D, E, and F, present a strain path in the right area of the FLD, typical of plane strains, but the recorded stress and strain values are very low respect to the elements closer to the hole edge.

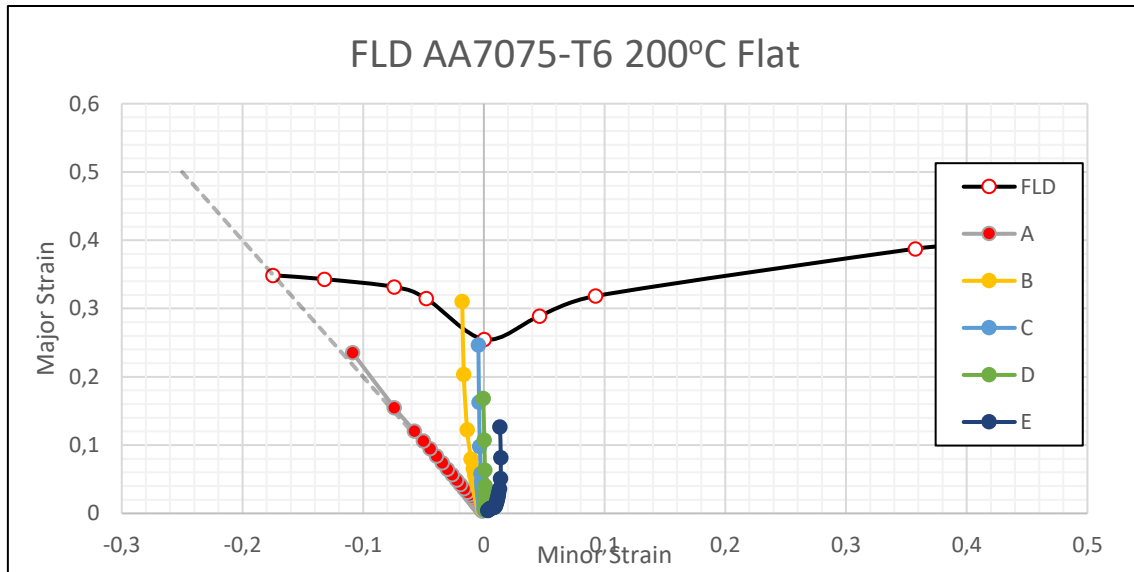


Figure 40 - Strain path of Conical Expansion, 200°C, from the hole edge (point A) to the punch shoulder (point F). The element labels refer to Figure 25b (FLD source: Sotirov et al. (2012)).

The recorded triaxiality at the time of the predicted failure (Figure 41) does not differ much from that recorded during the room temperature simulation. The elements on the hole edge present triaxiality values around 0.33, typical of uniaxial load (yellow color in Figure 41). The elements on the hole edge that present a uniaxial stress, are bounded by a plane strain triaxiality values (range from 0.4 to 0.6, orange in Figure 41) that represents the most dangerous condition in the strain plane. Negative triaxiality values are recorded in the layers of the workpiece in contact with the die corner and the punch fillet, as already stated, these values generally delay the onset of necking, although the strain state in these elements is very low compared to the rest of the blank, as shown in Figure 40 for elements E and F (labels refer to figure 25b).

Unfortunately, it was not possible to compare strain evolution vs triaxiality due to the lack of experimental data to define the MCC failure *locus* at elevated temperature, as instead was done for the case at room temperature.

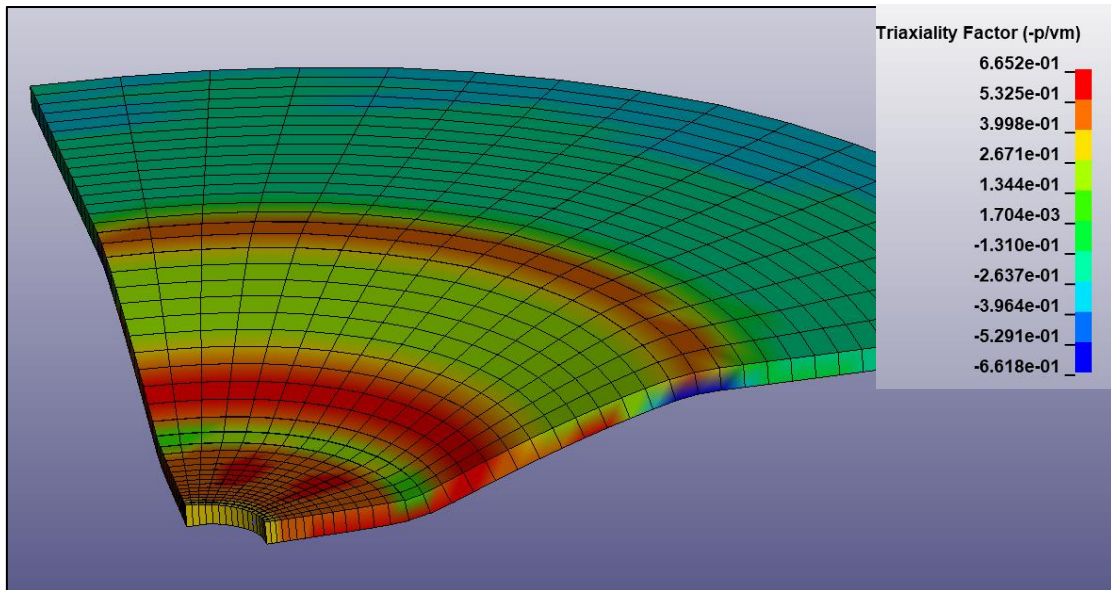


Figure 41- Contour of stress triaxiality within the workpiece on the flat expansion, 200°C.

5.3 Punch force vs displacement

Figure 42 shows the punch force exchanged with the workpiece versus the punch displacement for all the simulations.

As expected, the warming condition requires a lower amount of force for the same amount of deformation compared to the room temperature condition, or in other words, with the same energy it is possible to reach a higher punch displacement, and then a higher deformation state within the workpiece. Although a significant work reduction is detected between the room and warm temperature in the flat expansion, just a small work reduction is noticed when the temperature of the workpiece increases in the conical case. The reason why the temperature conditions affect more the expansion with the flat punch rather than the conical one is mostly related to the geometry of the test and how the different parts of the assembly come into contact with each other; in fact, in the flat case, the surface of the contact blank-punch is much larger than in the conical one.

Figure 42 shows also that the applied force on the workpiece in the flat expansion is almost four times larger than in the conical expansion. The reason for these results is mostly related to the amount of surface of the workpiece in contact with the punch in the flat expansion respect the conical one.

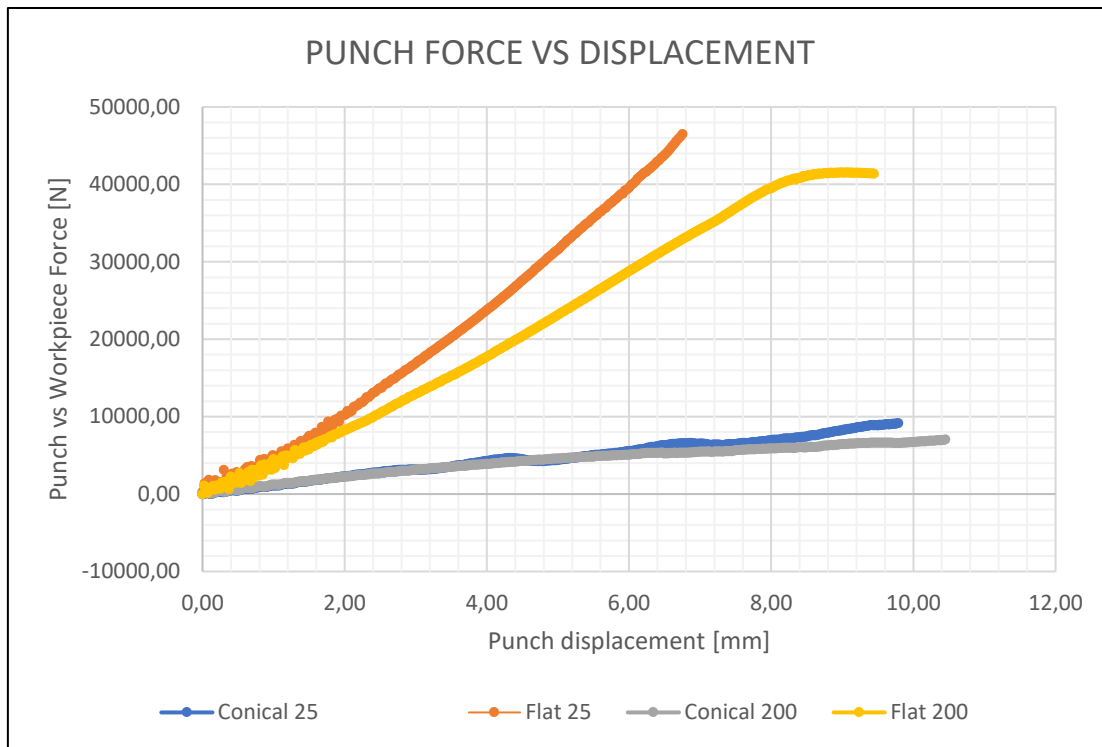


Figure 42- Force exchanged between the punch and the workpiece vs the punch displacement considering different punches and temperatures

5.4 Correlation of Hole Expansion with Tensile Properties

Extensive work has been done over the years to relate the results of the HER with the tensile properties of the materials. Various regression equations are available in the literature to predict HER. In this section, different regression equations are discussed, and their predictive capabilities are also compared with the properties of the AA7075-T6.

Adamczyk and Michal (1986) had developed some graphical and mathematical relations between the Hole Expansion Ratio and the average Lankford value and/or material transversal elongation. The reason why these two parameters are often related to the Hole Expansion Ratio is that they reflect the ability of the material to resist thinning.

In Figure 43 it possible to see the results of the predicted Hole Expansion Ratio in the conical configuration for the AA7075-T6 and the transversal total elongation of the material. In Figure 43 it is also possible to compare the HER results with several HSLA sheets.

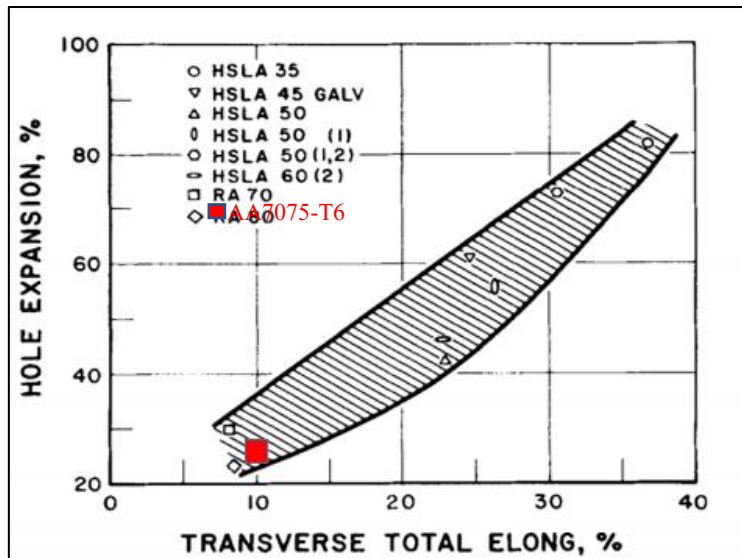


Figure 43- Effect of transverse total elongation on percent hole expansion. AA7075-T6 data based on the Rahmaan et al. (2016) characterization effort. (Picture source: Adamczyk & Michal, 1986).

Among the various relation proposed among the hole expansion, r_m , and transverse total elongation, the following simple functional relationship (Equation 6.7) produced a very good fit with the material tested by Adamczyk and Michal (1986):

$$HER (\%) = 15 + 1.7 * r_m * Tran.Total El. (\%) = 30.3\% \quad (6.7)$$

in good agreement with the predicted results of conical expansion (28.5%).

In Figure 44 the relationship between Equation 6.7 (considering various values of the Lankford coefficient) and the predicted Hole Expansion Ratio in the conical simulation at room temperature is reported.

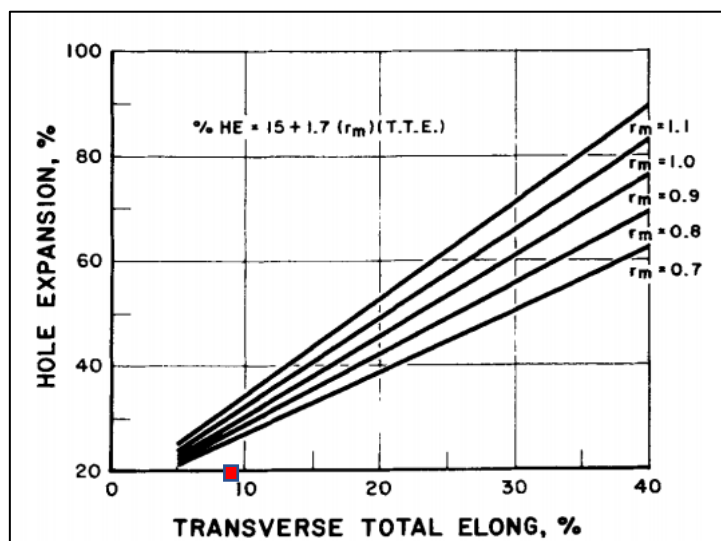


Figure 44 - Effect of r_m and transverse total elongation on percent hole expansion from linear regression analysis. AA7075-T6 data based on the Rahmaan et al. (2016) characterization effort. (Picture source: Adamczyk & Michal, 1986).

Manikandan *et al.* (2012) tried to correlate the ratio between Yield Strength and Ultimate Tensile Strength linearly, although the correlation of the data is not very accurate for the most of the materials examined by them, the predicted results from the simulation of AA7075-T6 at room temperature and 200°C are pretty close to the suggested straight line of Figure 45.

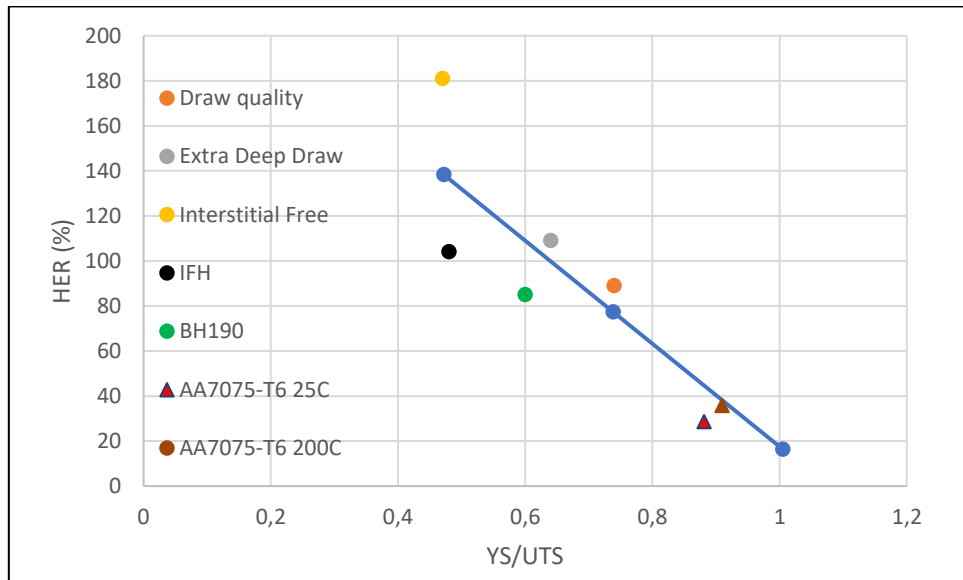


Figure 45- Relation between tensile strength and HER of AA7075-T6 with various steel tested by Manikandan *et al.* (2012). AA7075-T6 data based on the Rahmaan *et al.* (2016) characterization effort.

Also, Paul (2014b) tried to relate the tensile properties of a variety of materials with their Hole Expansion Ratio. In Figures 46a and 46b, there are reported the results of the materials analyzed in his research integrated with the HER predictions of this work. In this case too, the correlation between the data set can be considered satisfactory.

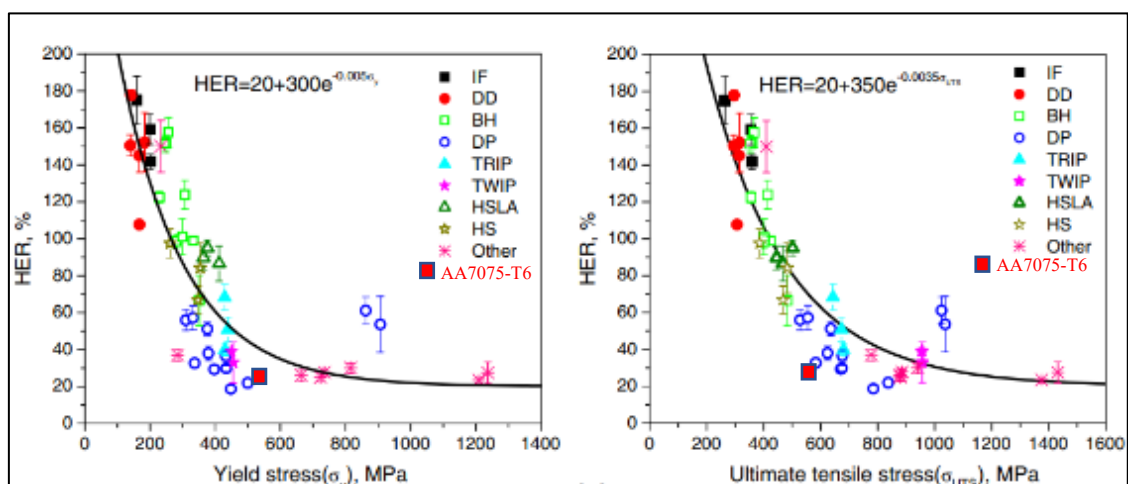


Figure 46 - Correlation between HER (%) and tensile properties of AA7075-T6 and a variety of other materials: a) yield stress, MPa. b) ultimate tensile stress, MPa. AA7075-T6 data based on the Rahmaan *et al.* (2016) characterization effort. (Picture source: Paul, 2014b).

6 CONCLUSIONS & FUTURE WORK

In this section, the main conclusions of this work are reported and briefly discussed, as is the proposed future work aimed to characterize the edge stretchability of AA7075-T6.

6.1 Conclusions

In this work, the stretch-flangeability of cold-rolled AA7075-T6 sheet was investigated by means of hole expansion simulations in different test conditions, including different punches and temperatures.

Finite element simulations of the hole expansion test were carried out using LS-DYNA. Forming limit stress curves, which are generated from experimental strain-based forming limit diagrams and mapped to stress space using von Mises yield function, were used for failure prediction.

Moreover, FE simulations showed that at the end of the test, both in the conical and the flat case expansion, at the hole edge is present a uniaxial tensile mode and that the strain evolution along the circumferential direction is comparable to the strain path that is recorded within the uniaxial tensile test sample until necking.

The deformation modes generated by the expansion operation within the blank are drawing next to the hole edge and stretching away from it. Between these two zones, just some millimeters away from the hole is present a “ring” with a plane-strain deformation, a very important zone in the flat-punch expansion; in fact, materials with intrinsically low ductility, e.g. AA7075-T6, are more suitable to show a plane strain failure away from the hole that will enhance their general hole expansion results.

Although the behavior of the material around the hole edge might be comparable to the one recorded during the uniaxial tensile test, not all the tensile properties are correlated with the HER of various materials present in the literature. These results, if supported by future experimental test, confirms the observations present in the literature that correlations between HER and the material tensile properties are only valid for a specific steel/aluminum groups having similar microstructure or strength grades, so it is not possible to generalize the results. It is especially important to note that parameters as n , m , and R , that are generally associated with the formability of the material, do not seem to strongly affect the HER of AA7075, as they do with other aluminum groups; this suggests a damaging process mostly controlled by the fracture, which is strictly related to

the microstructure of the material. Nevertheless, the predicted results of AA7075-T6 are in agreement with the regression analysis proposed by Adamczyk *et al.* (1986) where the HER varies linearly with the transverse total elongation of the material, as shown in Figure 43 and 44.

Even the small post uniform elongation recorded in uniaxial tests of the T6 temper looks to be one of the most influential parameters affecting the final HER, as it represents the material's ability to delay the fracture after diffuse necking (generally assumed as failure condition in FLD), in strong agreement with the findings of Paul *et al.* (2014a) that showed how the HER is strongly affected by the post-uniform elongation; experimental data is needed to confirm these relation.

Moreover, as reported by Pathak (2018), the damage induced in the material during the punching of the hole strongly affects the final HER. Although the induced damage of the punching process is not taken into account in the simulation model, according to the results presented in the literature and those in this work, it should affect more the conical expansion rather than the flat one. This is because the conical expansion has the blank-punch contact area and consequently the most of the deformation concentrated on the hole edge, while in the flat expansion, the punch exchanges forces with the blank through a wider surface, characterized by a transition from stretching to drawing along the radial direction with high plane-strain values in the region between (plane-strain corresponds to the minimum of FLC), having the most dangerous condition some millimeters away from the hole edge, where the effects of the SAZ are lower or absent. Then, the proposed simulation model and the predicted HER, should be considered as an upper limit of the hole expansion reachable in absence of damage (SAZ) due to the hole punch, a similar condition can be obtained with a high-quality hole cut (CNC Machining, milling and reaming, etc.) or through annealing after punching in order to remove the work-hardening present in the material (Butcher *et al.*, 2014).

The hole expansion simulations confirm the effect of punch shape and temperature on the test. The punch shape affects the stress state and consequently the location of the failure in the workpiece, while the temperature affects mostly the instant of the failure instead of its position, postponing the onset of the failure.

For the conical expansion, it is confirmed by MCC failure *loci*, qualitative FLD analysis, and thickness distribution, that the most critical elements leading to the through-thickness

crack in the workpiece are on the edge; on the contrary, the same analysis conducted on the flat punch expansion, showed that the most critical state is manifested some millimeters away from the hole edge, in a zone corresponding to the transition from uniaxial to plane strain deformation.

The consequence of this difference is reflected in the final HER when the test is carried out with the flat punch, lower values are recorded respect to those obtained with the conical punch, both at room and warm temperatures.

As expected, with increasing temperature at which the test is performed, the HER ratio is predicted to slightly increases; this increment is mostly due to the improved ductility of the material at warm temperatures that postpone the onset of diffuse necking and subsequent cracking in the material in comparison to the room temperature test.

6.2 Future work

The following future work is proposed as the next steps to support the characterization of shear edge sensitivity of AA7075-T6:

- Due to COVID-19 it has not been possible to carry out physical experiments to validate directly the model proposed in simulations. Future work should consider carrying out the experimental work on the material in order to validate the model and obtain the real HER for the various conditions, including various test temperatures and different punch shapes.
- The experimental work should also investigate the effect of the shearing process on the final HER; a particular interest should be directed to the effect of different shearing clearances and different hole shearing processes.
- The proposed model considers only 2 millimeters thickness for the AA7075-T6 sheets due to the lack of enough data to predict the failure with other thicknesses. Future work should consider how sheet thickness affects the HER and if it is possible to generalize its effect on other materials.
- The experimental work should define the induced damage on the blank generated during the shear operation. It would be important to investigate the effect and distribution of the damage due to the punching of the hole considering various punching clearances and have a comparison with other hole introduction techniques.

- The FE model does not include a failure criterion. Basing on experimental data, future works should investigate the most appropriate failure criteria to predict the HER in AA7075-T6.

Bibliography

- Adamczyk, R. D., & Michal, G. M. (1986). Sheared edge extension of high-strength cold-rolled steels. *Journal of Applied Metalworking*, 4(2), 157-163.
- Bai, Y., & Wierzbicki, T. (2008). A New Model of Metal Plasticity and Fracture With Pressure and Lode Dependence. *International Journal of Plasticity*.
- Banabic, D. (2010). *Sheet Metal Forming Processes*. Springer.
- Banhart, J. (2016). Metallurgy of heat treatable alloys. In *Heat Treating of Nonferrous Alloys* (pp. 214 - 239). ASM International.
- Barlat, F., Brema, J., J.W., Y., Chungd, K., Dicke, R., Lege, D. J., . . . Chu. (2003). Plane stress yield function for aluminum alloy sheets - part 1: theory. *International Journal of Plasticity* (19), 1297–1319.
- Bohdal, L., Kulakowska, A., & Patyk, R. (2014). Analysis of Slitting of Aluminum Body Panels in the Aspect of Scrap Reduction. *Rocznik Ochrona Srodowiska*.
- Carle, D., & Blount, G. (1999). In *Material & Design* (pp. 267-272).
- Considerere, A. (1885). Ann. Ponts et Chaussees 9.
- Davies, R. (1983). Edge cracking in high strenght steels. *Journal of Applied Metalworking*, 2 (4), 293 - 299.
- Ducker. (2017). *ALUMINUM CONTENT IN NORTH AMERICAN LIGHT VEHICLES 2016 TO 2028*. Ducker Worldwide.
- EuroCarBody. (2016, October 18-20). Slide presentation of EuroCarBody prize 2016. Bad Nauheim, Germany.
- G., D. (2020, June 5). *Electric Vehicles (EVs): outlook for sales and aluminium demand*. Retrieved from Aluminium Insider: <https://aluminiuminsider.com/>
- Garret, R. P., Lin, J., & Dean, T. A. (2005). Solution Heat Treatment and Cold Die Quenching in Forming AA 6xxx Sheet Components : Feasibility Study. In *Advanced Materials Research* (pp. 673 - 680).
- Golovashchenko, S. (2008). *Quality of trimming and its effect on stretch flanging in automotive pannels*.

- Golovashchenko, S., Hu, X. H., Choi, K. S., & Sun, X. (2014). Edge Fracture Prediction of Traditional and Advanced Trimming Processes for AA6111-T4 Sheets.
- Hooputra, H., Gese, H., Dell, H., & Werner, H. (2004). A Comprehensive Failure Model for Crashworthiness Simulation of Aluminium Extrusions. *International Journal of Crashworthiness*.
- <https://www.ilprogettistaindustriale.it/i-processi-che-tolgono-peso-e-migliorano-le-prestazioni-dellalfa-romeo-giulia/>. (2017). Retrieved from ilprogettistaindustriale.it.
- Hu, X. H., Sun, X., & Golovashchenko, S. F. (2016). An integrated finite element-based simulation framework: From hole piercing to hole expansion. *Elsevir*.
- ISO/TS. (2017). 16630:2017 Metallic materials - method of hole expansion test.
- Jones, R. M. (2009). *Deformation Theory of Plasticity*.
- Kacem, A., Krichen, A., Manach, P. Y., Thuillier, S., & Yoon, J. W. (2013). Failure prediction in the hole-flanging process of aluminium alloys. *Engineering Fracture Mechanics*, 99, 251–265.
- Kainer, K. U. (1998). “Potential von Magnesium in der Karosserie — Möglichkeiten und Entwicklungsbedarf. *Stahl, Aluminium und Magnesium im Wettbewerb, EUROFORUM-Konferenz*.
- Kaufman, G. J. (2000). *Introduction to Aluminium Alloys and Tempers*. ProQuest Ebook Central.
- Keeler, S. (1971). Understanding sheet metal forming. In *Part 5 - Die design and lubrication* (pp. 687 - 691). 1st ed Sheet Metal Industries.
- Konieczny, A., & Henderson, T. (2007). *On formability limitations in stamping involving sheared edge stretching*. SAE Technical Paper.
- Lankford, W. ..., Snyder, S. C., & Bauscher, J. A. (1950). New criteria for predicting the press performance of deep-drawing sheets. *Transtaction ASM* 42, 1196 - 1232.
- Lee, J., Ko, Y., Huh, H., Kim, H., & Park, S. (2007). Evaluation of hole flangeability of steel sheet with respect to the hole processing condition. *Key Engineering Materials*, 665 - 670.

- Levy, B., & Van Tyne, C. (2012). Review of the Shearing Process for Sheet Steels and Its Effect on Sheared-Edge Stretching. *Journal of the Mechanics and Physics of Solids*, 1020 - 1036.
- Li, M. (2000). An experimental investigation on cut surface and burr in trimming aluminum autobody sheet. *International Journal of Mechanical Science*, 889-906.
- Lloyd, D. J. (1999). DUCTILITY AND BENDABILITY IN 6000 SERIES AUTOMOTIVE ALLOYS. *Automotive Alloys*, 211 - 221.
- MacKenzie, D. S. (2016). Metallurgy of heat treatable aluminum alloys. In *ASM Handbook, volume 4E, Heat Treating of Nonferrous Alloys* (pp. 65 - 113). ASM International.
- Manikandan, G., Verma, R. K., & Paul, S. K. (2012). Finite Element Analysis of Hole Expansion Test for Various Cold Rolled. *International Deep Drawing Research Group (IDDRG) Conference*. Bombay.
- Marciniak, Z. a. (1967). Limit strains in the processes of stretch-forming sheet metal. *International journal of mechanical sciences*, 9(9), 609 - 620.
- Morris, L., & George, R. (1977). Warm Forming High-Strength Aluminum Automotive Parts. *SAE Technical Paper Series 770206*.
- Pathak, N. (2018). *Characterization and Modeling of Sheared Edge Failure in Advanced High Strength Steel*. Waterloo: UWaterloo.
- Pathak, N., Butcher, C., & Worswick, M. (2016). Assessment of the Critical Parameters Influencing the Edge Stretchability of Advanced High Strength Steel. *Journal of Materials Engineering and Performance*, 25 (11), 4919 - 4932.
- Paul, S. K. (2014b). Non-linear Correlation Between Uniaxial Tensile Properties and Shear-Edge Hole Expansion Ratio. *ASM International*, 3610-3619.
- Paul, S. K., Mukherjee, M., Kundu, S., & Chandra, S. (2014a). Prediction of hole expansion ratio for automotive grade steels. *Paul, S. K., Mukherjee, M., Kundu, S., & Chandra, S. (2014). Prediction of hole expansion ratio for automotive grade steels. Computational Materials Science*, 89, , 189–197.

- Rahmaan, T., Butcher, C., & Worswick, M. (2016). Constitutive Response of AA7075-T6 Aluminum Alloy Sheet in Tensile and Shear Loading. In *Experimental and Applied Mechanics. Volume 4* (pp. 115 - 122). Springer.
- Ramhaad, T. (2020). Private communication.
- Rice, J. R., & Tracey, D. M. (1969). On the ductile enlargement of voids in triaxial stress fields. *Journal of the Mechanics and Physics of Solids*.
- S., M. D. (2016). Metallurgy of het tratable aluminium alloys. In *Heat Treating of Nonferrous Alloys* (pp. 65 - 113).
- Seo, Y. (2003). Improving blank edge conditions. *Stamping journal*.
- Seo, Y. (2005). Blanking questions have you on the edge? *The fabricator*.
- Smith, D. (1990). Die design handbook. 1st ed. Dearborn, Mich.: Society of Manufacturing Engineers.
- Sotirov, N., Simon, P., Chimani, C., Uffelmann, D., & Melzer, C. (2012). Warm deep drawability of peak-aged 7075 aluminium sheet alloy. In *Key Engineering Materials, vol. 504* (pp. 955-960). Trans Tech Publ.
- Srivatsan , T. S., Sriram, S., Veeraraghavan, D., & Vasudevan, V. K. (1997). Microstructure, tensile defomration and fracture behaviour of aluminium alloy 7055. *Journal of materials science*.
- Stanton, M., Bhattachararya, R., Dargue, I., Aylmore, R., & Willams, G. (2011). Hole Expansion of Aluminium Alloys for the Automotive Industry. *The 14th International ESAFORM Conference on Material Forming*. American Insitute of Physics.
- Swift, H. (1952). Plastic instability under plane stress. *Journal of the Mechanics and Physics of Solids 1(1)*,, 1–18.
- Toros, S., Ozturk, F., & Kacar, I. (2008). Review of warm forming of aluminum-magnesium alloys. *J. Mater. Process. Technol*, vol. 207, no. 1–3, pp. 1–12,.
- van den Boogaard, A. H., Bolt, P., & Werkhoven, R. (2201). Aluminum sheet forming at elevated temperatures. *Simulation of Materials Processing: Theory, Method and Applications*, 819 - 824.

- Voce, E. (1955). A practical strain-hardening function. *Metallurgia*, 219-226.
- Wang, H., Luo, Y., Riedman, P., Chen, M., & Gao, L. (2001). Warm forming behavior of high strength aluminum alloy AA7075. *WANG, H., LUO, Y., FRIEDMAN, P., CHEN, M., & GAO, L. (2012). Warm forming behavior of high strength aluminum alloy AA7075. Transactions of Nonferrous Metals Society of China, 22(1), 1-7.*
- Wuyang, L., & Takashi, I. (2018). Trials to evaluate Lankford value using hole expansion test.
- Xue, L. (2005). *Damage Accumulation and Fracture Initiation in Uncracked Ductile Solids Under Triaxial Loading—Part I: Pressure Sensitivity and Lode Dependence, Impact and Crashworthiness*. Impact and Crashworthiness Laboratory, Massachusetts Institute of Technology, Cambridge, MA, Lab Report No. 138.
- Yu, Z., Lin, Z., & Zhao, Y. (2007). Evaluation of fracture limit in automotive aluminium alloy sheet forming, 28. In *Materials & Design* (pp. 203 - 207).